Thermodynamic model for metalorganic vapor-phase epitaxy of N-polar group-III nitrides in step-flow growth mode: Hydrogen, competitive adsorption, and configuration entropy

Takashi Hanada
Institute for Materials Research, Tohoku University, Sendai 980-8577, Japan

(Received 21 February 2019; revised manuscript received 18 July 2019; published 31 October 2019)

A thermodynamic model for metalorganic vapor-phase epitaxy (MOVPE) of the N-polar $(000\bar{1})$ binary group-III nitrides (AlN, GaN, and InN) in the step-flow growth mode is proposed based on the Burton, Cabrera, and Frank (BCF) theory. The coverages of the group-III adatoms are thermodynamically evaluated under competitive adsorption with hydrogen, which is used as a carrier gas or dissociated from the NH_3 source gas during MOVPE. The chemical potentials of the group-III and H adatoms on N-polar group-III nitride surfaces are modeled using the respective bond energies with the surface N atoms of the nitride and the vibrational frequencies of the adatoms. The coverages of the coadsorbed group-III and H adatoms are calculated using the Langmuir adsorption isotherm with these chemical potentials. The configuration entropy of the group-III adatoms bridges the gap between the thermodynamic model and the BCF theory. The coverage of the group-III adatoms plays a role like partial pressure of the group-III gas in the thermodynamics. The equilibrium coverage of the group-III adatoms and the equilibrium pressure of the NH_3 gas are evaluated from the conditions of Gibbs energy balance between the sources (group-III adatom and NH_3 gas molecule) and products (group-III nitride and $3/2$ H_2 gas molecules) and of speed balance between group-III and N incorporation into step kinks. Fair agreements with the experimentally optimized growth conditions for MOVPE of N-polar GaN and InN are obtained by this method. Among the examined binary group-III nitrides, AlN growth is hardly affected by H_2 gas pressure, GaN growth is controlled well by H_2 gas pressure, and InN growth is strongly inhibited by H_2 gas. A criterion for selecting the NH_3/group-III flow ratio for maximum products/cost and minimum waste of the materials is demonstrated using the growth model and the estimated growth parameters. The offcut angle dependence of the growth rate on the vicinal substrates is also investigated.

DOI: 10.1103/PhysRevMaterials.3.103404

I. INTRODUCTION

Growth techniques for epitaxial group-III nitrides using metalorganic vapor-phase epitaxy (MOVPE) have been developed with various applications in mind [1–6]. Conventional GaN-based devices are usually fabricated on the group-III-polar (0001) plane. However, novel devices on the N-polar $(000\bar{1})$ plane with opposite polarization field along the growth direction have recently attracted much attention because of the wider range of device structures and fabrication processes that then become available [7–9]. Control and identification methods for the polarity of GaN have been demonstrated on several kinds of substrates [10–13]. It has also been reported that the use of the N-polar $(000\bar{1})$ surface is effective in increasing the In incorporation ratio of InGaN [14,15]. Red-to-blue GaN-based LEDs have been demonstrated on the N-polar surface [16].

During MOVPE, H_2 is provided by NH_3 dissociation, even if it is not used as a carrier gas. It has been revealed using ion scattering that the N-polar *c*-plane GaN surface is covered with H adatoms, which are thermally segregated from H impurities in bulk GaN [17]. It has also been confirmed theoretically that the N-polar GaN and InN surfaces under an H_2 atmosphere are most stable when they are covered with $3/4$ or 1 monolayer H adatoms [18–20]. These results indicate that the equilibrium surfaces of the N-polar group-III nitrides consist of H adatoms and bare surface N atoms. It would be interesting to determine how the N-polar group-III nitrides grow on such surfaces. Thermodynamic analysis methods for the growth of compound semiconductors, including the group-III nitrides, were developed by Koukitu *et al.* [21]. They used the equilibrium constant expression between reactants (group-III and NH_3 gases) and products (group-III nitrides and H_2 gas). Recently, they have incorporated *ab initio* surface-energy calculations into the thermodynamic analysis and investigated the effect of growth orientation and surface reconstruction [19,20]. However, the kinetics of the minority group-III adatoms has not been explicitly treated in these methods. On the other hand, the Burton, Cabrera, and Frank (BCF) theory treats adatom diffusion on the growing surfaces and the kinetics at the steps and kinks [22–25].

In the present study, a calculation method for the MOVPE growth rate of N-polar AlN, GaN, and InN in the step-flow growth mode is proposed that is based on the BCF theory in combination with thermodynamic and statistical physics considerations. In this model, steady-state growth with continuous flow of the source gases and adatoms is considered using a modified version of the BCF theory, together with thermodynamic evaluation methods for the adatom densities and their equilibrium conditions. An extremely low density of the group-III adatoms on the N-polar growing surface under competitive adsorption of the group-III and hydrogen atoms is evaluated using the Langmuir adsorption isotherm model as a function of the partial pressures of the source gases at a given temperature [26,27]. In addition, the minimally

 ©2019 American Physical Society

required (equilibrium) coverage of the group-III adatom and the equilibrium pressure of NH_3 gas for the growth of the N-polar group-III nitride are estimated from the Gibbs free energy balance between the sources (group-III adatom and NH_3 gas) and the products (group-III nitride and $3/2$ H_2 gas). The low density of group-III adatoms is consistent with the very low nucleation rates of two-dimensional islands observed on N-polar GaN surfaces at a low degree of supersaturation [28]. In addition, competitive adsorption with H atoms suppresses condensation of the group-III adatoms. As a result, the H adatoms assist a moderate step-flow growth if a sufficient density of steps is provided on the growing surface. Many experiments have already revealed that the N-polar growth of a group-III nitride on a vicinal substrate, which has high-density steps, is preferred to prevent the formation of hexagonal pyramids and hillocks [8,9,29,30].

A recent theoretical study has confirmed that trimethylgallium (TMG) and trimethylindium, precursor gases used in MOVPE, are easily decomposed to monoatomic Ga and In gases, respectively, whereas trimethylaluminum reacts with NH_3 in the gas phase to form $(CH_3)_2AlNH_2$ [31]. In the present study, however, monoatomic Al gas as well as Ga and In gases is assumed as the source gas for the competitive adsorption with hydrogen. Therefore, the results for AlN will be presented just for comparison with the results for GaN and InN.

II. STEP-FLOW GROWTH MODEL AND ITS PROBLEMS

In the step-flow growth mode, adsorption, desorption, and migration of the adatoms on the terraces as well as the adatom incorporation into the steps and the kinks shown in Fig. 1 are the substantial processes. The growth rate in this mode can be quantitatively evaluated using the BCF theory [22–24]. In the present study, growth on a vicinal surface of an N-polar group-III nitride is exclusively treated. Therefore, steps are assumed to preexist. According to the vapor-growth model based on the BCF theory, the surface density c_j of the adsorbed species j obeys the following diffusion equation incorporating the adsorption and desorption rates:

$$\frac{\partial c_j}{\partial t} = D_j^s \nabla^2 c_j + F_j \Omega c_{\text{bare}} - \frac{c_j}{\tau_j}, \tag{1}$$

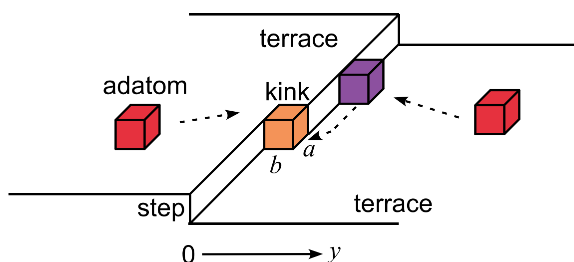

FIG. 1. Illustration of adatom migration on terraces and adatom incorporation into a step and a kink. Even if an adatom is incorporated into a kink, the total area of terraces, length of steps, and number of kinks are conserved. Therefore, advance of the kink corresponds to extension of the bulk.

where t is time, D_j^s is the surface diffusion coefficient, F_j is the adsorption rate per unit area, $\Omega = ab$ is the area of an adsorption site as shown in Fig. 1, c_{bare} is density of bare adsorption sites, and τ_j is the lifetime of the adatom. The adsorption sites form a lattice on a terrace. In the case of the wurtzite c plane, whose lattice constant is a, b is $\sqrt{3}a/2$ when the step is parallel to the a axis. In the standard BCF model, the total adatom density is assumed to be very small and Ωc_{bare} is unity. However, c_{bare} is explicitly introduced in the present study and Eq. (1) has been slightly modified from the standard model, because the adsorption density of the H adatoms c_{H} is not negligible on N-polar group-III nitrides during MOVPE. Also, consistency with the Langmuir adsorption isotherm [26,27], which quantifies the surface density of a specific species of adatoms as a function of the partial pressures at a given temperature, is provided by the introduction of c_{bare} and c_{H} as shown later. The incident flux F_j^0 of gas molecule j at its partial pressure p_j is

$$F_j^0 = p_j / \sqrt{2\pi m_j k_{\text{B}} T}, \tag{2}$$

where m_j is the mass of molecule j, k_{B} is Boltzmann's constant, and T is temperature. The adsorption rate can then be represented as

$$F_j = \eta_j F_j^0, \tag{3}$$

where η_j is the sticking coefficient of the incident molecule, which is less than unity. The coverage of the adatoms, i.e., the number of adatoms per surface area Ω, is

$$\theta_j(y) = \Omega c_j(y), \tag{4}$$

where y is the coordinate normal to the steps, as shown in Fig. 1. The adatom density is assumed to be uniform parallel to the steps on an ensemble average. The steady-state and uniform coverage of adatom j on an infinitely wide terrace is obtained as

$$\theta_j^\infty = \Omega F_j \tau_j \Bigg/ \left(\sum_i \Omega F_i \tau_i + 1 \right) \tag{5}$$

by substituting $\partial c_j / \partial t = 0$, $\nabla^2 c_j = 0$, and $\Omega c_{\text{bare}} = \theta_{\text{bare}} = 1 - \sum_i \theta_i$ into Eq. (1) and solving the simultaneous equations. Here j and i represent all kinds of adsorbed species, excluding the bare sites, on the terrace. This form is consistent with the Langmuir adsorption isotherm for the competitive adsorption as a function of the partial pressures [27], and the coverages never exceed unity, even at an extremely high p_j, in so far as this model is valid.

In MOVPE of N-polar group-III nitrides, the adsorbed species on the terraces are H and M (one of the group-III species). It must be noted that an H_2 molecule is dissociatively adsorbed as two H adatoms, and F_{H} in Eq. (5) is proportional to $\sqrt{p_{\text{H}_2}}$ [27,32]. The steady-state ($\partial c_M / \partial t = 0$) group-III adatom coverage between the equally-spaced parallel straight steps on an ideal vicinal surface is obtained from Eq. (1) in the range $0 < y < l_s$ as

$$\theta_M(y) = \theta_M^\infty - \left(\theta_M^\infty - \theta_M^{\text{eq}} \right) \frac{\cosh\left[(2y - l_s) / (2\lambda_M^s) \right]}{\cosh\left[l_s / (2\lambda_M^s) \right]}, \tag{6}$$

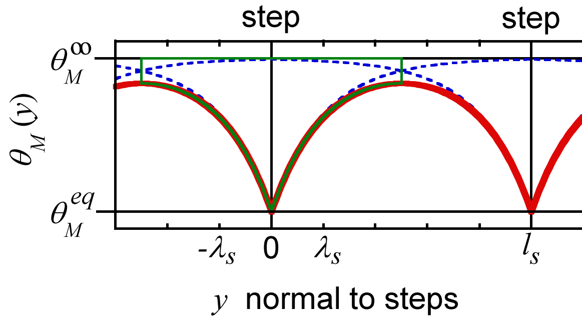

FIG. 2. Steady-state coverage of adatom M (red thick line) on the terraces between equally spaced parallel straight steps. θ_M^∞ is the coverage on an infinitely wide terrace, θ_M^{eq} is the coverage at the steps, l_s is the interstep distance, and λ_M^s $(= l_s/5)$ is the modified surface diffusion length of the adatom. The blue dashed lines are the coverage for a single step.

where θ_M^{eq} is the coverage of the adatoms M at the steps (i.e., the inlets of the adatoms into the crystal), l_s is the interstep distance, $\lambda_M^s = x_M^s/\sqrt{\Omega F_M \tau_M + 1} = x_M^s/\sqrt{\theta_M^\infty/\theta_{\mathrm{bare}}^\infty + 1}$, and $x_M^s = \sqrt{D_M^s \tau_M}$ is the surface diffusion length of the adatom [22,23]. The formula of Eq. (6) is the same as that of the standard BCF model, where $\theta_M^\infty = \Omega F_M \tau_M$ and $\lambda_M^s = x_M^s$ because $\Omega F_M \tau_M$ is assumed to be much smaller than unity. An example of $\theta_M(y)$ is shown by the red thick line in Fig. 2 for $\lambda_M^s = l_s/5$. The blue dashed lines are the coverage for a single step. The advance velocity υ_M of the steps is calculated from Eq. (6) as $\Omega D_M^s(\partial c_M/\partial y|_{y=+0} - \partial c_M/\partial y|_{y=-0})$, which is the product of Ω (if an adatom is incorporated at every step segment of length a, the step advances b) and the adatom diffusion-current density (per step length) into the step at $y = 0$ from the terraces on both sides [22,23]:

$$\upsilon_M = K_M\left(\theta_M^\infty - \theta_M^{\mathrm{eq}}\right), \tag{7}$$

where

$$K_M = \frac{2D_M^s}{\lambda_M^s} \tanh \frac{l_s}{2\lambda_M^s}. \tag{8}$$

The asymmetry of the adatom incorporation from the lower and the upper terraces to the step is ignored in the present study for simplicity. The relation

$$\upsilon_M = \frac{1}{\tau_M} \int_{-l_s/2}^{l_s/2} \left[\theta_M^\infty - \theta_M(y)\right] dy \tag{9}$$

is also easily confirmed from Eq. (6) and the periodicity of $\theta_M(y)$. This shows that the step velocity is identical to the area surrounded by the green closed line in Fig. 2 over the lifetime of the adatoms. The step is the inlet of the adatoms to the crystal. The coverage of the adatoms decreases from θ_M^∞ to $\theta_M(y)$ as a result of the existence of the steps. It can be seen from Eq. (9) that, in an ensemble average, the decreasing adatoms are incorporated to the crystal at the step during their lifetime.

Although the slight modification of the parameters θ_M^∞ and λ_M^s from the standard BCF model is easy as shown above, the quantitative evaluation method of the sticking coefficient, which is necessary to obtain θ_j^∞, under competitive adsorptions is not so obvious. Furthermore, in the case of group-III-nitride MOVPE growth, both nitrogen incorporation and the release of hydrogen from NH_3 must be reflected in θ_M^{eq}. To solve these problems, thermodynamic and statistical physics approaches are used to calculate both θ_j^∞ and θ_M^{eq} for N-polar group-III nitride growth. The evaluation of the adatom coverage θ_j^∞ under competitive adsorption with H is possible using the Langmuir adsorption isotherm based on Gibbs energy minimization for the adsorbed system [27], as shown in Appendix B and Sec. III B, instead of evaluating the sticking coefficient and the lifetime in Eq. (5). The equilibrium coverage θ_M^{eq} is evaluated in Sec. III C using the condition of Gibbs energy balance during crystallization from the group-III adatoms and the NH_3 gas molecules, as well as the speed balance between the incorporations of group-III and N atoms into the step kinks [33].

III. RESULTS AND DISCUSSION

A. Chemical potentials of related pure substances and adsorbed species

To study the thermodynamic relationships among the source gases, the released gases, the adatoms, and the group-III nitrides, their chemical potentials must be known. Except for the adatoms, their Gibbs free energy data were obtained from databases [34,35]. Figure 3 shows the chemical potentials as functions of temperature. In Fig. 3, the pressure of the gases is standard pressure ($p^\circ = 1$ bar) unless shown explicitly, and "bulk" denotes the solid and liquid phases of the group-III metals below and above their melting points, respectively. To estimate the bond energies and chemical potentials of the adsorbed species, the chemical potentials of the related gases, AlN, GaN, and InN are extrapolated as functions of T down to 0 K in the Supplemental Material I [36]. The chemical potential of gas j at partial pressure p_j is represented as

$$\mu_j^{\mathrm{gas}}(T, p_j) = \mu_j^{\circ\mathrm{gas}}(T) + k_{\mathrm{B}} T \ln(p_j/p^\circ), \tag{10}$$

where $\mu_j^{\circ\mathrm{gas}}(T)$ is the chemical potential at standard pressure [35,37–39].

The atomic structure of the N-polar GaN surface is illustrated in Fig. 4. Two types of step and kink and two types of Ga adsorption sites (T1 and B2) are shown. The T1 adatom *terminates one* surface N atom. The B2 adatom makes a *bridge* between *two* N atoms at the step of the N-polar surface [40]. Adsorption of N, NH, NH_2, and H at the site denoted by Gn, which is surrounded by n surface *Ga* atoms, will also be considered in Appendix C to determine the step and terrace structures. For example, NH adsorption at G3 and NH_2 adsorption at G2 are shown in Fig. 4. The adsorption sites can be represented as Sn, where S is T, B, or G and n is the number of the bonds at the site. The chemical potential of an adatom j ($= M$, H, or N, where M represents Al, Ga, or In) at the Sn site is modeled using the Helmholtz free energy of the harmonic

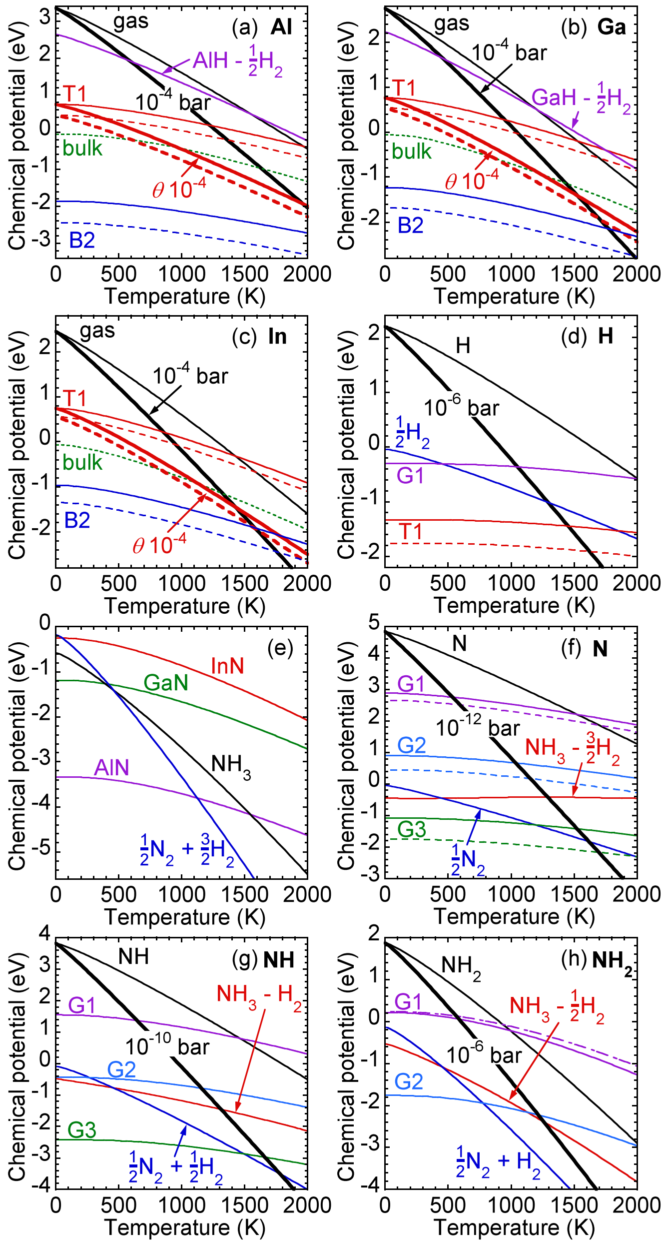

FIG. 3. Chemical potentials of related substances and adsorbed species as functions of temperature. The pressure of the gases is standard pressure (1 bar) and the coverage θ of the adsorbed species is unity unless these values are shown explicitly (thick lines). For instance, $NH_3-3/2H_2$ in (f) denotes $\mu^{\circ\mathrm{gas}}_{\mathrm{NH_3}} - 3\mu^{\circ\mathrm{gas}}_{\mathrm{H_2}}/2$. "bulk" denotes the solid and liquid phases of the group-III metals below and above their melting points. The adjustment factor γ_j^{Sn} in Eq. (11) for the bond energy of the adsorbed species j at the site Sn is assumed to be unity (dashed lines) or 0.9 (solid and chained lines). The vibrational temperatures cited from Ref. [41] are used for the chained line in (h).

oscillators as

$$\mu_j^{\circ Sn}(T) = \mu_j^{\circ\mathrm{gas}}(0) - n\gamma_j^{Sn}E_{j-s}^{\mathrm{bond}} + k_\mathrm{B}\sum_{i=1}^{n_j}\left\{\frac{\Theta_{ji}^{Sn}}{2} + T\ln\left[1-\exp\left(-\frac{\Theta_{ji}^{Sn}}{T}\right)\right]\right\}, \tag{11}$$

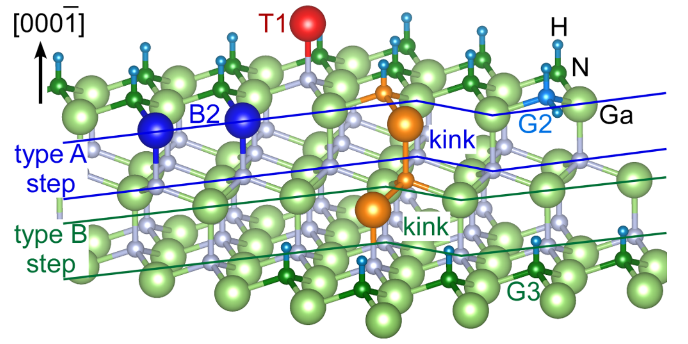

FIG. 4. Schematic atomic structure of the N-polar GaN $(000\bar{1})$ surface under a hydrogen atmosphere with the double-step (type-A and type-B) structure perpendicular to $\langle 10\bar{1}0\rangle$. T1-Ga (red), B2-Ga (blue), and T1-H (small cyan) adatoms are shown. NH and NH_2 adsorbed on three Ga (G3) and two Ga (G2) atoms, respectively, are also shown.

where $\mu_j^{\circ\mathrm{gas}}(0)$ is the enthalpy of gaseous j at 0 K, $\gamma_j^{Sn}E_{j-s}^{\mathrm{bond}}$ is the single-bond energy between atom j and surface atom s ($s = \mathrm{N}$ or M), and Θ_{ji}^{Sn} is the vibrational temperature of mode i [39,41]. The number of vibrational modes n_j is three for a monatomic adatom. The results of the extrapolations in the Supplemental Material I [36] are used only to estimate $\mu_j^{\circ\mathrm{gas}}(0)$ and the reference value of the bond energy E_{j-s}^{bond} in the bulk group-III nitrides and NH_3 gas. The adjustment factor γ_j^{Sn} is introduced because the actual bond energy between the adatom and the surface atom is different from E_{j-s}^{bond}. The Θ_{ji}^{Sn}s of the adatom are estimated in the Supplemental Material II [36]. The superscript open circle on the left-hand side of Eq. (11) indicates the exclusion of the configuration entropy due to the freedom of adatom location. As shown in Appendix A, the configuration entropy of each adsorbed species depends on the coverage θ_j^{Sn}, which is the occupancy ratio of the adatom j at the Sn sites. Hereinafter, a dangling bond without any adsorbate ($j = \mathrm{bare}$) is treated as a kind of adsorbate. The consequent coverage-dependent chemical potentials of M and H adatoms and the dangling bonds at the T1 sites are

$$\mu_j^{\mathrm{T1}}\left(T, \theta_j^{\mathrm{T1}}\right) = \mu_j^{\circ\mathrm{T1}}(T) + k_\mathrm{B}T\ln\theta_j^{\mathrm{T1}}, \tag{12}$$

where $\mu_{\mathrm{bare}}^{\circ\mathrm{T1}}(T)$ is zero and $\sum_j \theta_j^{\mathrm{T1}}$ is unity. The coverage, including that of the dangling bonds, plays a role like the partial pressure of gas in Eq. (10). The relationships between the adatoms and the dangling bonds are like those between electrons and holes. All of the adatoms and the dangling bonds diffuse from their respective high-coverage regions to low-coverage regions to decrease their free energies. In other words, diffusion (random walk) is an irreversible process and proceeds to increase entropy. In the BCF theory, a steady current of group-III adatoms to the steps is created owing to the decreasing coverage toward the steps shown in Fig. 2. Furthermore, the configuration entropy of the T1 adatoms is consistent with a rate equation like Eq. (1), because the transition rate from a position with coverage θ_j^{T1} is proportional to $\theta_j^{\mathrm{T1}}\exp[-E_A/(k_BT)] = \exp[-(E_A - k_BT\ln\theta_j^{\mathrm{T1}})/(k_BT)]$, where E_A is the activation energy of an adatom. From the right-hand side of the equation,

it is regarded that the coverage-dependent activation energy increases with decreasing coverage because of the decrease in the free energy of the initial state. The adsorption in Eq. (1) can be regarded as a desorption of the bare state.

The coverage-dependent chemical potentials at the B2 and Gn sites are given in Appendix A. The chemical potentials of the adsorbed species calculated using the parameters in the Supplemental Material I and II [36] are shown in Fig. 3 by dashed lines assuming $\gamma_j^{\mathrm{T1}} = 1$ and by solid lines assuming $\gamma_j^{\mathrm{T1}} = 0.9$. It will be shown in Secs. III D and III E that the use of the reduced γ_j^{T1} for the T1 adatoms provides better agreement with experimental results.

B. Coverages of adsorbed species

The coverages of the adatoms at the T1 and B2 sites for the binary competitive adsorption of H_2 and M are calculated using Eqs. (B2a)–(B2c) in Appendix B. The coverages as functions of T and p_{H_2} assuming $\gamma_j^{Sn} = 1$ (dashed line) and 0.9 (solid line) are shown in Figs. 5 and 6. In most cases, the coverage of H (Al, Ga, In, and dangling bonds) decreases (increases) on reduction of γ_j^{Sn}, because the difference in bond energy between H and the group-III adatoms decreases. Under typical MOVPE growth conditions, T1 sites are almost all occupied with H adatoms. As a result, the coverage of the group-III adatoms at the T1 sites becomes very low, as shown in Fig. 5, and their chemical potential decreases to be lower than or similar to that of the bulk group-III metal, as shown in Figs. 3(a)–3(c). The coverage $\theta_{\mathrm{bulk}}^{\mathrm{eq}}$ of the group-III adatoms in equilibrium with the bulk metal, where their chemical potentials are the same, is shown by green lines in Fig. 5. If $\theta_M^{\mathrm{T1}\infty}$ is smaller than $\theta_{\mathrm{bulk}}^{\mathrm{eq}}$, then condensation of the group-III atoms to bulk is prevented by the lower chemical potential of the adatoms. The coverage of the group-III adatoms decreases with increasing temperature and increasing p_{H_2}. If the T, p_M, and p_{H_2} conditions are the same, the coverage of Al is highest and that of In is lowest among the three group-III atoms. This is consistent with the strength of the respective bonds with the surface N atoms. For the B2 sites, the group-III atoms almost occupy these sites at the usual growth temperature, as shown in Fig. 6. Therefore, the group-III atoms at the type A step edge shown in Fig. 4 can be considered to be stable. The condensation of the B2 adatoms to the bulk group-III metal is prevented owing to the lower chemical potential shown in Figs. 3(a)–3(c). The occupancy ratio of H decreases further to that of an impurity if n increases to 4 in bulk group-III nitrides.

The coverages of N, NH, NH_2, and H at the G1, G2, and G3 sites were also calculated under the competitive dissociative adsorption of NH_3 and H_2. The details of the calculation are given in Appendix C. The coverages as functions of T, p_{H_2}, and p_{NH_3} are shown in Fig. 7, assuming $\gamma_j^{Sn} = 0.9$. The calculated coverage of H at the G1 sites was about 0.003 and those of NH_x ($x = 0,\ 1$, and 2) are less than 10^{-7} under typical MOVPE growth conditions for GaN (not shown). This is consistent with the fact that the chemical potential of the NH_x adsorbates at the G1 site shown in Figs. 3(f)–3(h) is higher than the difference of those between the source NH_3 and the released H_2 gases (red lines). This result suggests that the bare Ga atoms appear at the type B step edges, as shown in Fig. 4. The results in Figs. 7(a)–7(c) show that the G2 sites are almost empty and even the coverage of NH_2 is less than 0.1 under the typical MOVPE growth conditions for GaN. This suggests that mostly bare B2 Ga adatoms appear at the type A step edges, as shown in Fig. 4. On the other hand, Figs. 7(d)–7(f) show that the G3 sites on the terraces are almost filled with NH or N. Therefore, Figs. 5–7 more or less support the illustration of the terrace and step structures shown in Fig. 4 for N-polar GaN under the typical growth conditions, although the parameters γ_j^{Sn} and Θ_{ji}^{Sn} in Eq. (11) need to be more accurately evaluated in the future. In the following sections, only the coverages of Al, Ga, In, and H at the T1 sites are used. Therefore, a qualitative evaluation is sufficient for the coverages at other sites.

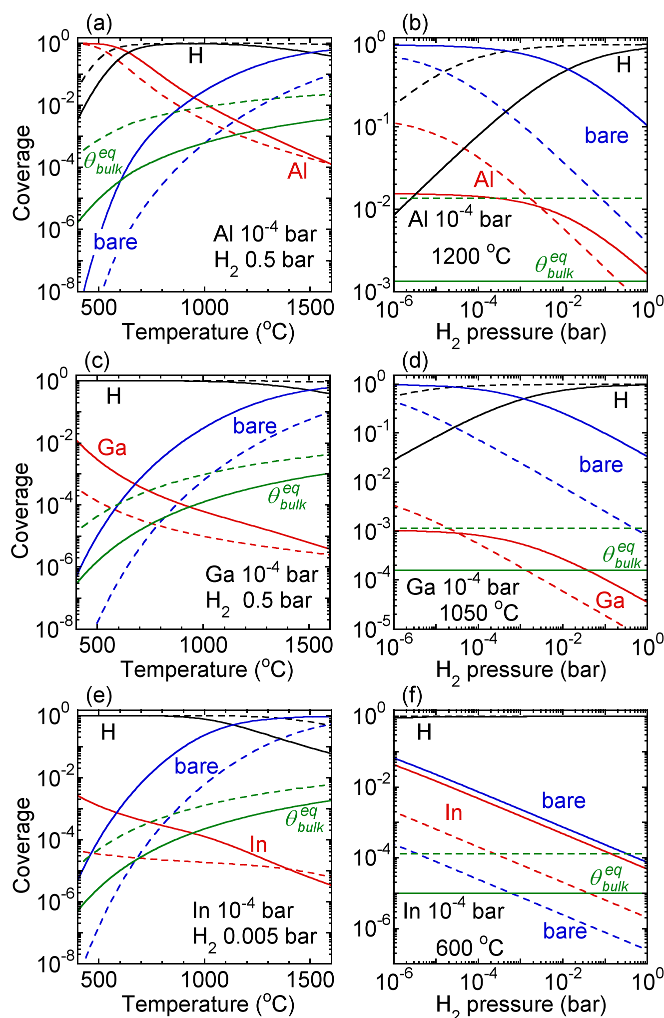

FIG. 5. Coverages of the Al (a) and (b), Ga (c) and (d), and In (e) and (f) adatoms at the T1 sites as functions of temperature and H_2 pressure for binary competitive adsorption of group-III gas at 10^{-4} bar and H_2 gas. The fixed parameters are indicated in each frame. The adjustment factor γ_j^{Sn} is unity (dashed lines) or 0.9 (solid lines).

Finally, we briefly discuss the applicability of the minimum-free-energy coverages at the T1 and B2 sites to the N-polar growth model. It is considered that the adsorptions at the T1 sites have a greater chance to reach the minimum free energy than those at the B2 sites owing to the ease of

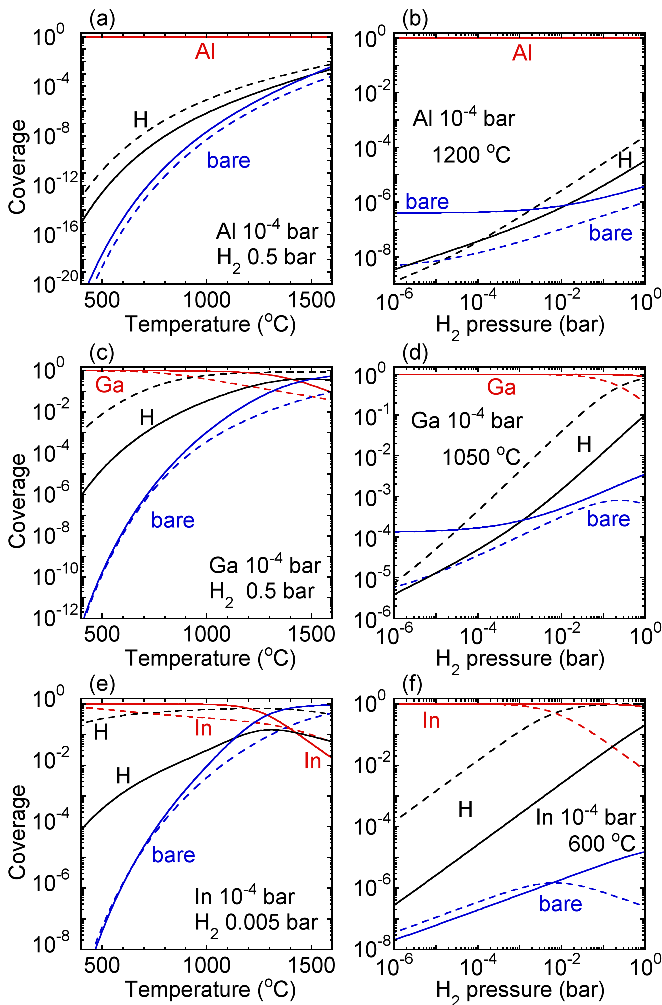

FIG. 6. Same as Fig. 5, but for the B2 sites.

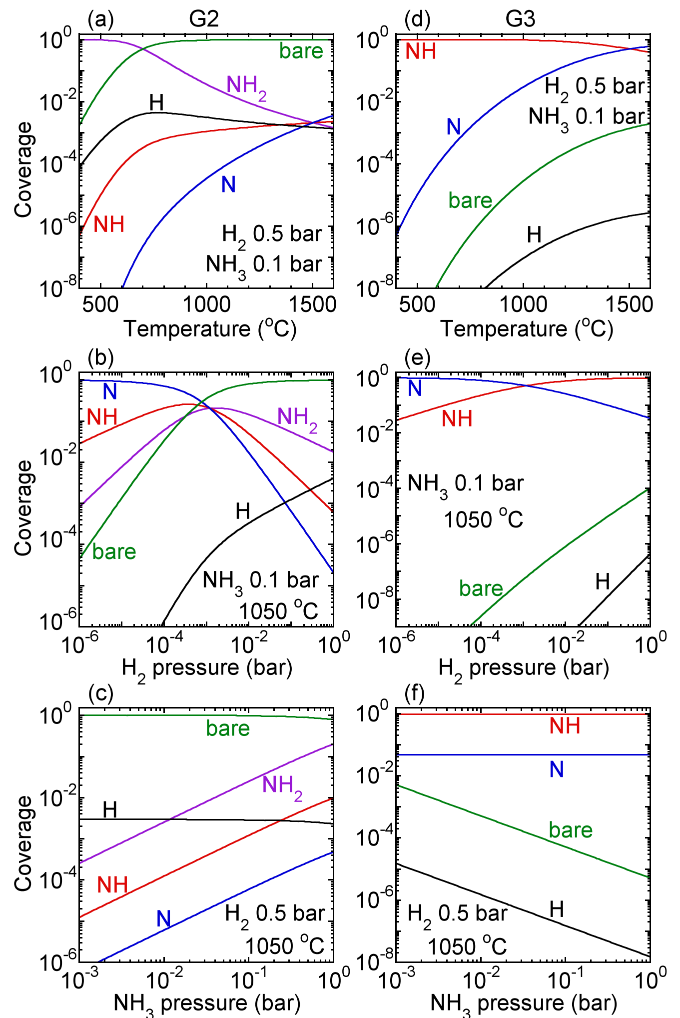

FIG. 7. Coverages of the adsorbed species at the G2 (a)–(c) and G3 (d)–(f) sites as functions of temperature (a) and (d), H_2 pressure (b) and (e), and NH_3 pressure (c) and (f) for competitive adsorption of NH_3 and H_2 gases. The fixed parameters are indicated in each frame. The adjustment factor γ_j^{Gn} is 0.9.

desorption, which enables repeated adsorption. The B2 sites on the N-polar surface appear only at the kinks and steps, which are the growth front. Therefore, the lifetime of each B2 site is relatively short, and it is possible that the B2 sites are embedded in the growing layers before their adsorbates reach the minimum-free-energy distribution. In this way, the occupancy ratio of the adsorbates is probably governed by kinetics with an increasing number of bonds n at an adsorption site. In the next section, we assume that the incorporation of the T1 group-III adatoms into the kinks is the main route for N-polar group-III nitride growth in the step-flow growth mode. It will be also confirmed in Sec. III E that direct incorporation of the group-III atoms at the kinks from gas is not enough to reproduce the observed growth rate.

C. Equilibrium growth condition and growth rate

On the c-plane surfaces, there are two types of low index step edges perpendicular to $\langle 10\bar{1}0\rangle$, type A and type B steps, as shown in Fig. 8 [29]. On the N-polar (group-III-polar) surface, a group-III (nitrogen) atom along the type A step edge has two backbonds and two dangling bonds, while a group-III (nitrogen) atom along the type B step edge has three backbonds and only one dangling bond. The type A step may grow if a group-III adatom is fixed at any step-edge position by the adsorption of NH into the G3 site illustrated in purple. This process also provides two additional kinks. On the other hand, two group-III adatoms must join together to be stable along the type B step, as shown by red atoms. Therefore, the type A step advances faster than the type B step and catches up with the lower type B step to form a double step of height c, as illustrated in Fig. 4 [29]. It has been reported that N-polar GaN actually grows with double steps [28]. If the catch-up process is rapidly finished in a very early stage of the epitaxial growth, the double-step growth will be steady during the rest of the growth. In this case, the type A step also proceeds only at kinks, because step edges are limited by the lower type B step and there is no lower terrace for the type A step, as shown in Fig. 4. Therefore, we assume that the growth-rate defining process of the N-polar growth in the step-flow growth mode is the advance of the double kink in Fig. 4.

Incorporation of an MN pair at a kink is equivalent to extending bulk MN [22,25]. That is to say, if there is no change in the local step and kink structure except for the

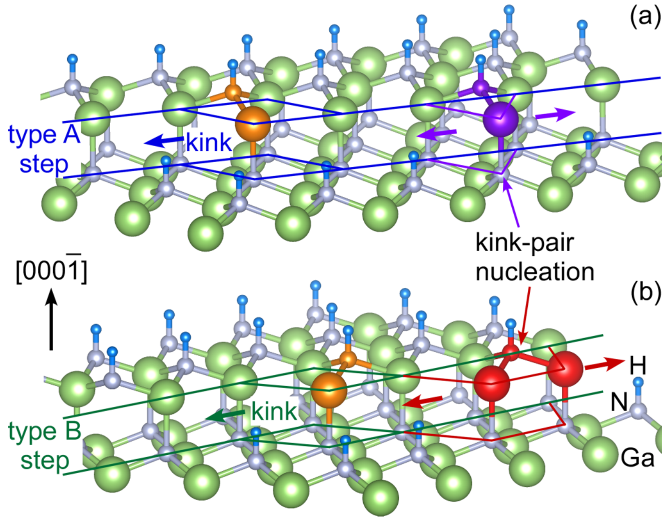

FIG. 8. Schematic atomic structure of the N-polar GaN surface with type-A (a) and type-B (b) step-and-kink structures under a hydrogen atmosphere. The steps are perpendicular to $\langle 10\bar{1}0\rangle$. The Ga–N pairs incorporated at the kinks are shown in orange. Possible initial structures to create kinks at the type-A and the type-B steps are shown in purple and red, respectively.

advance of the kink position (toward the left in Figs. 4 and 8) after the incorporation of the MN pairs (orange atoms), then the surface, step, and kink energies are conserved. Therefore, the increase in the Gibbs energy of the nitride due to the incorporation of an MN pair at a kink is identical to the bulk $\mu_{MN}(T)$. This is also true if the annihilation and creation of kinks illustrated in Fig. 9(a) are balanced and the kink density is conserved during the growth. The incorporation process at a kink can be divided into four elementary actions as follows:

(i) A group-III T1 adatom migrates into a kink from the terrace.

(ii) An NH_3 molecule impinges on the newly formed G3 site.

(iii) The NH_3 is dissociatively adsorbed as NH and two H atoms are transferred to the neighboring Ga atoms at the step edge.

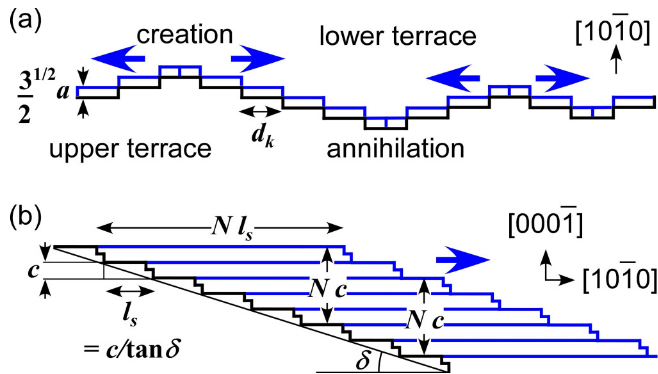

FIG. 9. (a) Schematic top view of a simplified kink advance, annihilation, and creation during unit step advance in the m direction. (b) Cross-sectional view of a simplified double-step (height c) advance for growth of thickness Nc on the vicinal substrate of off-angle δ. The directions of advance are indicated by the thick blue arrows.

(iv) The two H atoms and the H atom replaced by the group-III adatom in (i) will be associatively desorbed as 3/2 H_2 molecules ($3H_2$ molecules for the double kink).

While actions (ii) and (iii) are occurring, the next action (i) into the advanced kink position can proceed in parallel. Also, the H_2 release at action (iv) and the adsorption of the group-III adatoms on the terraces proceed in parallel during the M and N incorporation in actions (i)–(iii). Four M–N bonds, which is identical to the number of bonds per bulk MN pair (each atom has four bonds and a bond is shared by two atoms in bulk), are formed by these actions. The decrease in the Gibbs energy during actions (i)–(iv) is expressed as

$$\begin{aligned}\Delta G(\theta_M^{\rm T1}, p_{\rm NH_3}) &= \mu_M^{\rm T1}(T, \theta_M^{\rm T1}) + \mu_{\rm NH_3}^{\rm gas}(T, p_{\rm NH_3})\\ &\quad - \mu_{MN}(T) - \frac{3}{2}\mu_{\rm H_2}^{\rm gas}(T, p_{\rm H_2})\\ &= \Delta G_M + k_{\rm B}T\ln\left(\frac{\theta_M^{\rm T1} p_{\rm NH_3} p^{\circ 1/2}}{p_{\rm H_2}^{3/2}}\right), \end{aligned}\quad (13)$$

where

$$\Delta G_M = \mu_M^{\circ\rm T1}(T) + \mu_{\rm NH_3}^{\circ\rm gas}(T) - \mu_{MN}(T) - \tfrac{3}{2}\mu_{\rm H_2}^{\circ\rm gas}(T). \quad (14)$$

The dependence of ΔG_M on AlN, GaN, and InN as a function of T is shown in Fig. 10(a).

The equilibrium (minimally required) values of the M-adatom coverage $\theta_M^{\rm T1eq}$ and the NH_3 pressure $p_{\rm NH_3}^{\rm eq}$ at the kinks, above which MN grows, satisfy the condition $\Delta G(\theta_M^{\rm T1eq}, p_{\rm NH_3}^{\rm eq}) = 0$, i.e.,

$$\theta_M^{\rm T1eq} p_{\rm NH_3}^{\rm eq} = \frac{p_{\rm H_2}^{3/2}}{p^{\circ 1/2}}\exp\left(-\frac{\Delta G_M}{k_{\rm B}T}\right). \quad (15)$$

In this case, a degree of supersaturation can be defined as

$$\begin{aligned}\sigma_c &= \left(\theta_M^{\rm T1\infty} p_{\rm NH_3} - \theta_M^{\rm T1eq} p_{\rm NH_3}^{\rm eq}\right)/\left(\theta_M^{\rm T1\infty} p_{\rm NH_3}\right)\\ &= 1 - \frac{p_{\rm H_2}^{3/2}}{\theta_M^{\rm T1\infty} p_{\rm NH_3} p^{\circ 1/2}}\exp\left(-\frac{\Delta G_M}{k_{\rm B}T}\right)\\ &= 1 - \exp\left[-\Delta G\left(\theta_M^{\rm T1\infty}, p_{\rm NH_3}\right)/(k_{\rm B}T)\right], \end{aligned}\quad (16)$$

which converges to unity at large $\theta_M^{\rm T1\infty} p_{\rm NH_3}$.

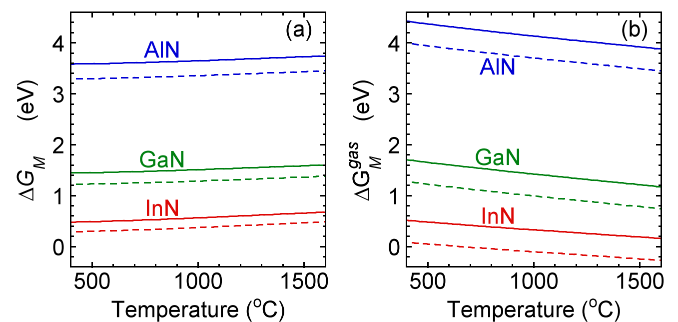

FIG. 10. (a) ΔG_M defined by Eq. (14) and (b) $\Delta G_M^{\rm gas}$ defined by Eq. (28) of AlN, GaN, and InN as functions of temperature. The adjustment factor $\gamma_j^{\rm T1}$ is unity (dashed lines) or 0.9 (solid lines).

The velocity of advance of the step due to the incorporation of the M adatoms in action (i) is given by Eq. (7) as

$$\upsilon_M = K_M^{\mathrm{ads}}\left(\theta_M^{\mathrm{T1}\infty} - \theta_M^{\mathrm{T1eq}}\right), \tag{17}$$

where the parallel incorporation of N into the kinks will be taken into account later. K_M^{ads} is obtained from Eq. (8) as

$$K_M^{\mathrm{ads}} = \frac{D_M^s}{\lambda_M^s}\tanh\frac{l_s}{2\lambda_M^s}, \tag{18}$$

where K_M is divided by two because M adatoms supplied from the upper and lower terraces of the double step are shared by the type A and type B steps. It is assumed that the mean distance between adjacent kinks in Fig. 9(a), d_k, is sufficiently less than both l_s and x_M^s. Then, an adatom is rapidly incorporated into a nearby kink after its arrival at a step.

Similarly, the velocity of advance of the step due to the incorporation of N in actions (ii) and (iii) can be expressed as

$$\upsilon_{\mathrm{N}} = K_{\mathrm{NH_3}}^{\mathrm{gas}}\left(p_{\mathrm{NH_3}} - p_{\mathrm{NH_3}}^{\mathrm{eq}}\right), \tag{19}$$

where $K_{\mathrm{NH_3}}^{\mathrm{gas}}$ is the kinetic coefficient for NH_3 incorporation from gas. $K_{\mathrm{NH_3}}^{\mathrm{gas}}$ can be expressed as

$$K_{\mathrm{NH_3}}^{\mathrm{gas}} = \frac{\Omega^2 \eta_{\mathrm{NH_3}}}{d_k\sqrt{2\pi m_{\mathrm{NH_3}} k_{\mathrm{B}} T}}, \tag{20}$$

where $\eta_{\mathrm{NH_3}}$ is the sticking probability of the incident NH_3 into a bare G3 site formed by action (i). Equation (20) is obtained as follows: first, the incident NH_3 flux from Eq. (2) is multiplied by the area Ω of the kink and by $\eta_{\mathrm{NH_3}}$ to evaluate the number n_k of N atoms incorporated during the successive kink advances per unit time; next, the step advances $\Omega n_k/d_k$ during the kink advance by an_k, because every step advances $\sqrt{3}a/2$ in the m direction if every kink advances d_k, as shown in Fig. 9(a).

The two velocities υ_M and υ_{N} must be the same [33]. For example, if υ_M is larger than υ_{N}, the leftover M adatoms will return to the terraces and θ_M^{T1eq} will increase. That is to say, the current of the M adatoms on the terraces into the kinks will decrease until $\upsilon_M = \upsilon_{\mathrm{N}}$ is satisfied. The equilibrium condition of Eq. (15) and this condition provide θ_M^{T1eq} and $p_{\mathrm{NH_3}}^{\mathrm{eq}}$ individually as

$$\theta_M^{\mathrm{T1eq}} = \frac{1}{2K_M^{\mathrm{ads}}}\left(\sqrt{\Delta^2 + Q} + \Delta\right) \tag{21a}$$

and

$$p_{\mathrm{NH_3}}^{\mathrm{eq}} = \frac{1}{2K_{\mathrm{NH_3}}^{\mathrm{gas}}}\left(\sqrt{\Delta^2 + Q} - \Delta\right), \tag{21b}$$

respectively, where

$$\Delta = K_M^{\mathrm{ads}}\theta_M^{\mathrm{T1}\infty} - K_{\mathrm{NH_3}}^{\mathrm{gas}} p_{\mathrm{NH_3}} \tag{22a}$$

and

$$Q = 4K_M^{\mathrm{ads}}K_{\mathrm{NH_3}}^{\mathrm{gas}}\frac{p_{\mathrm{H_2}}^{3/2}}{p^{\circ 1/2}}\exp\left(-\frac{\Delta G_M}{k_{\mathrm{B}}T}\right). \tag{22b}$$

The step velocity is then obtained as

$$\upsilon_{\mathrm{step}} = \upsilon_M = \upsilon_{\mathrm{N}} = \frac{2u_M u_{\mathrm{N}}}{u_M + u_{\mathrm{N}} + \mathrm{sgn}(\sigma_c)\sqrt{(u_M + u_{\mathrm{N}})^2 - 4u_M u_{\mathrm{N}}\sigma_c}}, \tag{23}$$

where the elemental velocities defined as

$$u_M = K_M^{\mathrm{ads}}\theta_M^{\mathrm{T1}\infty}\sigma_c \tag{24a}$$

and

$$u_{\mathrm{N}} = K_{\mathrm{NH_3}}^{\mathrm{gas}} p_{\mathrm{NH_3}}\sigma_c \tag{24b}$$

are introduced to distinguish whether the growth condition is M limited or N limited. Although u_{N} is inversely proportional to d_k, u_M is independent of d_k as long as $d_k \ll x_M^s$, because the supply of the M adatoms from the terraces is shared by nearby kinks. When σ_c is negative (evaporation), K_M^{ads} and $K_{\mathrm{NH_3}}^{\mathrm{gas}}$ are different from those in Eqs. (18) and (20), respectively. Furthermore, $\upsilon_M = \upsilon_{\mathrm{N}}$ is not assured. Therefore, σ_c is limited to be positive in the present study. The step velocity given by Eq. (23) is smaller than both u_M and u_{N}, and is limited by the smaller of the two. Figure 11 shows the step velocity normalized by u_M as a function of u_{N}/u_M at various σ_c values. Here u_M and u_{N} are interchangeable, because the step velocity of Eq. (23) is a symmetric function of them. If the steps proceed in the form of a double step, then the thickness of the c-plane film increases by c after each step advances by l_s, as shown by the case of $N = 1$ in Fig. 9(b). Therefore, the growth rate in the thickness direction is

$$\upsilon_{\mathrm{thick}} = \frac{c}{l_s}\upsilon_{\mathrm{step}}. \tag{25}$$

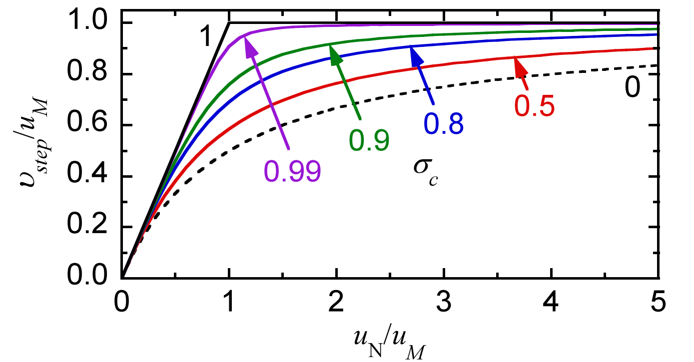

FIG. 11. Step velocity normalized by u_M as a function of u_{N}/u_M at the indicated σ_c values. The subscripts M and N can be interchanged. Care must be taken in comparison with experiments: if the flow rate of NH_3 is increased while that of TMG is kept constant, then σ_c increases.

D. Group-III-gas-pressure representation of equilibrium growth condition

The crystal grows only if σ_c is positive, which is equivalent to the condition

$$\theta_M^{\mathrm{T1}\infty} p_{\mathrm{NH_3}} > \frac{p_{\mathrm{H_2}}^{3/2}}{p^{\circ 1/2}} \exp\left(-\frac{\Delta G_M}{k_{\mathrm{B}}T}\right). \tag{26}$$

The use of p_M in place of $\theta_M^{\mathrm{T1}\infty}$ is much more convenient. This replacement is possible if the coverage of the H adatom is approximately known. By taking the ratio between Eqs. (B2a) and (B2b) in Appendix B, the necessary condition in Eq. (26) for growth is rewritten as

$$p_M p_{\mathrm{NH_3}} > \frac{p_{\mathrm{H_2}}^2}{\theta_{\mathrm{H}}^{\mathrm{T1}\infty}} \exp\left(-\frac{\Delta G_M^{\mathrm{gas}}}{k_{\mathrm{B}}T}\right), \tag{27}$$

where

$$\Delta G_M^{\mathrm{gas}} = \mu_M^{\circ\mathrm{gas}}(T) + \mu_{\mathrm{NH_3}}^{\circ\mathrm{gas}}(T) + \mu_{\mathrm{H}}^{\circ\mathrm{T1}}(T) - \mu_{M\mathrm{N}}(T) - 2\mu_{\mathrm{H_2}}^{\circ\mathrm{gas}}(T). \tag{28}$$

Similarly, σ_c is rewritten as

$$\sigma_c = 1 - \frac{p_{\mathrm{H_2}}^2}{p_M p_{\mathrm{NH_3}} \theta_{\mathrm{H}}^{\mathrm{T1}\infty}} \exp\left(-\frac{\Delta G_M^{\mathrm{gas}}}{k_{\mathrm{B}}T}\right). \tag{29}$$

This shows that the equilibrium condition for growth is not explicitly affected by errors in $\mu_M^{\circ\mathrm{T1}}(T)$ but only by those on $\mu_{\mathrm{H}}^{\circ\mathrm{T1}}(T)$ and $\theta_{\mathrm{H}}^{\mathrm{T1}\infty}$. The dependence of $\Delta G_M^{\mathrm{gas}}$ on AlN, GaN, and InN is shown in Fig. 10(b). The condition in Eq. (27) indicates that the product of the source pressures necessary to grow MN increases proportionally to the square of the H_2 pressure. This is a very severe requirement for InN growth, since the $\Delta G_M^{\mathrm{gas}}$ of InN is smaller than those of AlN and GaN as shown in Fig. 10(b). Therefore, N_2 is usually used as a carrier gas during MOVPE growth of InN and InGa(Al)N [3]. The equilibrium condition for $p_M p_{\mathrm{NH_3}}$, i.e., the right-hand side of Eq. (27), is calculated at various values of $p_{\mathrm{H_2}}/\sqrt{\theta_{\mathrm{H}}^{\mathrm{T1}\infty}}$ as a function of temperature and shown in Figs. 12(a)–12(c). For each value of $p_{\mathrm{H_2}}/\sqrt{\theta_{\mathrm{H}}^{\mathrm{T1}\infty}}$, the growth rate is zero on the corresponding line, and the N-polar MN grows only above the line. We have examined the calculations assuming $\gamma_{\mathrm{H}}^{\mathrm{T1}} = 1$ (dashed lines) and $\gamma_{\mathrm{H}}^{\mathrm{T1}} = 0.9$ (solid lines). Only the latter results agree fairly well with those of GaN and InN growth experiments. This suggests that the N–H bond of the H adatom is weaker than that of NH_3. In the case of AlN growth, use of H_2 carrier gas imposes practically no limitation on the growth, because the calculated equilibrium conditions are extremely low at the usual H_2 pressures. The use of H_2 carrier gas at around 1 bar is also suitable for N-polar GaN growth at the usual growth temperatures around 1000 °C, Ga pressure around 10^{-5} bar, and NH_3 pressure around 1 bar. Furthermore, precise control of the H_2 flow rate can adjust the H_2 pressure to be slightly above the equilibrium growth condition, which is favorable for step-flow growth without kinetic roughening. On the other hand, N_2 carrier gas has been used to grow InN. Even when this is done, H_2 is produced by dissociation of NH_3. The solid lines in Fig. 12(c) indicate that the pressure of H_2 should be lower than about 0.1 bar at the usual growth temperatures around 600 °C, In pressure around 10^{-4} bar, and NH_3 pressure around 1 bar.

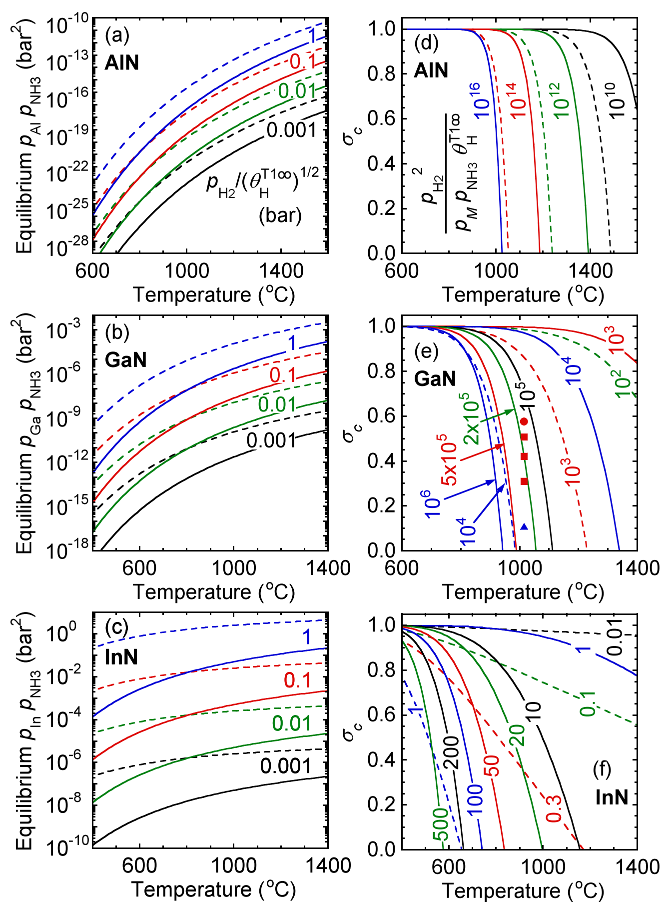

FIG. 12. (a)–(c) Equilibrium $p_M p_{\mathrm{NH_3}}$ for N-polar MN growth in the ideal step-flow growth mode (M = Al, Ga, and In) as a function of temperature calculated at the four $p_{\mathrm{H_2}}/\sqrt{\theta_{\mathrm{H}}^{\mathrm{T1}\infty}}$ values indicated in each frame. ΔG is zero on each line, and the N-polar MN grows above the line. (d)–(f) Degree of supersaturation σ_c for N-polar III-nitrides as a function of temperature at the various $p_{\mathrm{H_2}}^2/(p_M p_{\mathrm{NH_3}} \theta_{\mathrm{H}}^{\mathrm{T1}\infty})$ values indicated in each frame. The points where σ_c falls to zero correspond to equilibrium, $\Delta G = 0$. The symbols in (e) correspond to the growth conditions of Ref. [42] (see Sec. III E). All the curves are independent of the chemical potential of the group-III T1 adatoms. The adjustment factor $\gamma_{\mathrm{H}}^{\mathrm{T1}}$ is unity (dashed lines) or 0.9 (solid lines).

In the case of GaN and InN growth, growth rate limitation at high temperature is chiefly caused by σ_c. In Figs. 12(d)–12(f), σ_c is shown as a function of temperature at various values of the pressure-ratio parameter $p_{\mathrm{H_2}}^2/(p_M p_{\mathrm{NH_3}} \theta_{\mathrm{H}}^{\mathrm{T1}\infty})$ for $\gamma_{\mathrm{H}}^{\mathrm{T1}} = 1$ (dashed lines) and $\gamma_{\mathrm{H}}^{\mathrm{T1}} = 0.9$ (solid lines). The points where σ_c falls to zero correspond to equilibrium. Similar temperature dependence of the growth rate [21] and of the stability of the InN surface structures [19] has been reported in previous thermodynamic analyses. In the case of AlN, σ_c is almost always unity regardless of temperature and H_2 pressure under typical growth conditions. The extremely large pressure-ratio parameters for AlN indicated in Fig. 12(d) are selected to show the falls in σ_c. Although σ_c is unity even at extremely small pressures of Al and NH_3, their pressures

need to be sufficiently high to obtain a practical growth rate. Therefore, it is likely that AlN usually grows under a highly supersaturated condition. MOVPE growth of GaN is usually performed at growth temperatures of 900–1100 °C and pressure-ratio parameters from about 10^4 to 10^6. Under these growth conditions, N-polar GaN growth near the equilibrium condition is possible only if $\gamma_{\rm H}^{\rm T1} = 0.9$ is assumed, as shown in Fig. 12(e). For InN, N_2 carrier gas is used. If the pressures of In, NH_3, and H_2 created by the decomposition of NH_3 are 10^{-4}, 1, and 0.1 bar, respectively, and the H-adatom coverage is almost unity, the pressure-ratio parameter is 100. Under these conditions, if $\gamma_{\rm H}^{\rm T1} = 0.9$, then InN growth is possible below 740 °C, as shown in Fig. 12(f) by the solid line marked with 100. The NH_3 decomposition ratio and the H_2 pressure probably increase with temperature.

E. Comparison between experimental and calculated results

Group-III-source flow-rate modulation epitaxy (FME) of N-polar GaN has been developed by Lin *et al.* [42] to improve the flatness of the growing surface. In this section, fair agreement with their experimental results will be shown, assuming $\gamma_{\rm H}^{\rm T1} = 0.9$. In their experiment, the growth temperature was 1015 °C, the reactor pressure was 0.400 bar, and the input flow rates of H_2 and NH_3 were 10 slm (standard liter per minute) and 0.067 mol/min, respectively. The input flow rates of TMG was 21 μmol/min during the high-flow period and 10 μmol/min during the low-flow period. The decomposition ratio α (0 to 1) of the NH_3 input flow, where a fraction $1-\alpha$ of NH_3 remains and a fraction α is decomposed to 1/2 N_2 and 3/2 H_2, is introduced in the calculations following Refs. [19–21]. The pressures of H_2, NH_3, N_2, and Ga are assumed to be proportional to their flow rates (or that of TMG for Ga) after NH_3 decomposition has occurred. In the case of $\alpha = 0$, the H_2 and NH_3 pressures are 0.348 and 0.052 bar, respectively. The Ga pressure is 1.64×10^{-5} bar during the high-flow-rate period and 0.78×10^{-5} bar during the low flow-rate period. At these pressures $\theta_{\rm H}^{\rm T1\infty}$ is 0.96 and $\theta_{\rm bare}^{\rm T1\infty}$ is 0.04 [43]. During the high- (low-) flow-rate period, $\theta_{\rm Ga}^{\rm T1\infty}$ is 1.13×10^{-5} (5.40×10^{-6}) if $\gamma_{\rm Ga}^{\rm T1} = 0.9$, ΔG is $0.86k_{\rm B}T$ ($0.12k_{\rm B}T$), and σ_c, which is plotted by a circle (a triangle) in Fig. 12(e), is 0.58 (0.11). Even in the case of $\alpha = 0.3$, $\theta_{\rm H}^{\rm T1\infty}$ and $\theta_{\rm bare}^{\rm T1\infty}$ are almost unchanged and $\theta_{\rm Ga}^{\rm T1\infty}$ decreases only slightly to 1.08×10^{-5} (5.13×10^{-6}). However, $p_{\rm H_2}^2/(p_{\rm Ga}p_{\rm NH_3}\theta_{\rm H}^{\rm T1\infty})$ increases and σ_c decreases with increasing α. In the cases of $\alpha = 0.1,\ 0.2,$ and 0.3, σ_c in the high-flow-rate period is shown by squares in Fig. 12(e), while σ_c in the low-flow-rate period decreases to become negative. Very slow spiral growth of the N-polar GaN is possible under the same growth condition as in the low-flow-rate period [28]. This suggests that σ_c is positive even in the low-flow-rate period, and consequently α is less than 0.078, where σ_c becomes zero, with the assumption of $\gamma_{\rm H}^{\rm T1} = 0.9$. Under the FME growth condition, $\theta_{\rm Ga}^{\rm T1\infty}/\theta_{\rm bulk}^{\rm eq}$ is about 0.08. Therefore, condensation of the Ga adatoms into bulk Ga is prevented.

The estimated σ_c values suggest that GaN grows sufficiently above the equilibrium condition during the high-flow-rate period and near the equilibrium condition during the low-flow-rate period. Therefore, some irregular structures with excess step and kink energies can be formed during the high-flow-rate period because there is a margin to allow incorporation of MN in a situation with larger chemical potential than the bulk $\mu_{M\rm N}$ in Eq. (13). However, if the low flow rate of TMG is carefully adjusted as in the experiment of Lin *et al.* [42], these irregular structures become unstable and may disappear during the low-flow-rate period. On the other hand, the steps grown by advance of the regular kinks are more stable, even during the low-flow-rate period. These results suggest that H_2 is a suitable carrier gas for well-controlled N-polar GaN growth near the equilibrium condition. It is expected that H_2 FME is also possible to improve flatness.

Next, it must be confirmed that the observed growth rate of 1.52–2.04 μm/h [42] can be reproduced using properly estimated kinetic coefficients. The observed growth rates correspond approximately to double-layer growth per single high-flow-rate period (1 s), $c/{\rm s} = 3600\ c/{\rm h} = 1.87\ \mu{\rm m/h}$. We will try to reproduce this rate. Lin *et al.* [42] used an N-polar GaN substrate with 0.3° offcut toward the m plane. In this case, l_s in Eqs. (18) and (25) is about 99 nm. Therefore, $\upsilon_{\rm step}$ must be 99 nm/s. Every double step advances l_s in a single cycle of FME. After 1800 cycles have been repeated, the terrace at the highest edge of the sample surface extends as wide as $1800l_s = 178\ \mu$m without any step deriving from the initial vicinal surface, as shown by the case of $N = 1800$ in Fig. 9(b). In this stepless area, N-polar GaN may grow in the spiral growth mode around threading screw dislocations [28]. Although this small area on the whole 10×5 mm^2 substrate may be neglected, annihilation of kinks during growth is not negligible and creation of kinks needs to occur at the same rate to maintain the kink density as shown schematically in Fig. 9(a). Kink creation may start from the formation of irregular Ga–N units, shown in Fig. 8 by red and purple, when Ga adatoms fail to seek a nearby kink, particularly along the long straight segments of the step. The rate of kink creation and the density $1/d_k$ of kinks along a step may be high at high σ_c, which allows the formation of irregular Ga–N units.

From Eqs. (18) and (24a),

$$u_{\rm Ga} = \frac{\theta_{\rm Ga}^{\rm T1\infty}}{\tau_{\rm Ga}}\sigma_c x_{\rm Ga}^s \tanh\frac{l_s}{2x_{\rm Ga}^s} \tag{30}$$

is obtained, where $\lambda_{\rm Ga}^s$ is replaced with $x_{\rm Ga}^s$ because $\theta_{\rm Ga}^{\rm T1\infty} \ll \theta_{\rm bare}^{\rm T1\infty}$. The lifetime of the Ga adatom is

$$\tau_{\rm Ga} = \nu_{\rm stretch}^{-1}\exp\left(E_{\rm Ga}^{\rm des}/k_{\rm B}T\right), \tag{31}$$

where $E_{\rm Ga}^{\rm des}$ is the energy barrier for Ga-adatom desorption and $\nu_{\rm stretch}$ is the frequency of Ga-adatom bond stretching [22–24]. The surface diffusion coefficient of the Ga adatom is

$$D_{\rm Ga}^s = a^2\nu_{\rm bend}\exp\left(-E_{\rm Ga}^{\rm diff}/k_{\rm B}T\right), \tag{32}$$

where $E_{\rm Ga}^{\rm diff}$ is the energy barrier for Ga-adatom diffusion and $\nu_{\rm bend}$ is the frequency of Ga-adatom bond bending [22–24]. In these calculations, the vibrational temperatures estimated in the Supplemental Material II [36] are converted into frequencies. $E_{\rm Ga}^{\rm des}$ is tentatively assumed to be given by

$$E_{\rm Ga}^{\rm des} = \gamma_{\rm Ga}^{\rm T1}E_{\rm Ga\text{-}N}^{\rm bond} - k_{\rm B}\sum_{i=1}^{3}\frac{\Theta_{{\rm Ga}i}^{\rm T1}}{2}\coth\left(\frac{\Theta_{{\rm Ga}i}^{\rm T1}}{2T}\right), \tag{33}$$

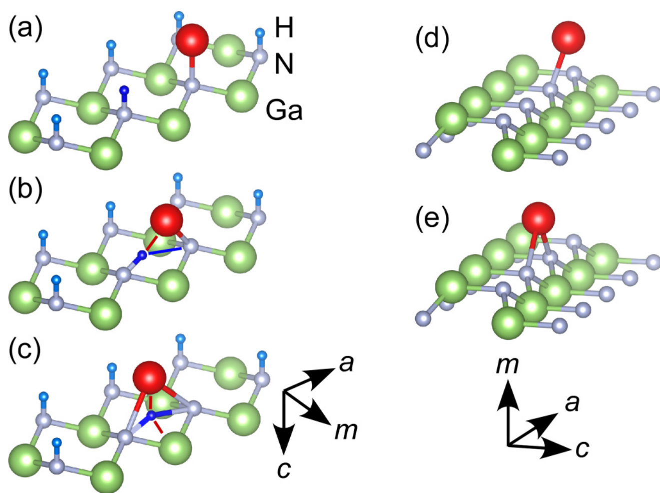

FIG. 13. Schematic structures of a Ga adatom (red) and H adatoms (blue) at the T1 sites (a), and possible Ga and H configurations at the intermediate position (b) and at the saddle-point position (c) in the course of site exchange on the N-polar GaN surface. Schematic structures of Ga adatom (red) at the T1 site (d) and at the saddle-point position (e) in the course of migration on the *m*-plane GaN surface [44].

where the internal energy due to the vibrations of the Ga adatom is subtracted from the unknown bond energy of the Ga adatom. Another unknown parameter is $E_{\mathrm{Ga}}^{\mathrm{diff}}$. The T1 sites on terraces are almost filled with H adatoms. Even if the coverage of the bare sites is 1/4 [17–20], it is difficult for the Ga adatom to reach a kink through a path consisting of only bare sites, because the percolation threshold density on a triangular lattice is 0.5. This suggests that the Ga adatom migrates by site exchange with neighboring H adatoms. Figure 13 illustrates a possible adatom motion from initial (a), intermediate (b), to saddle point (c) during the site exchange. The diffusion barrier of the Ga T1 adatom in the *a* direction on the *m*-plane GaN surface has been calculated as 0.21 eV [44]. The Ga-adatom motion on the *m* plane is shown in Figs. 13(d) and 13(e). The bond length and the angles between the bonds around the Ga adatom and around the first-neighbor N atoms are different from those of the bulk in the saddle-point configuration shown in Fig. 13(e) [44]. Therefore, the bonding energy of the Ga adatom in Fig. 13(e) is much lower than that of the B2 adatom in Fig. 4. The configurations around the Ga adatoms shown in Figs. 13(a) and 13(d) are the same to the second neighbor of the adatom if the slight difference in the bond along the *c* axis of the wurtzite structure is ignored. Also, those in Figs. 13(c) and 13(e) are the same except for the H atom below the adatom in Fig. 13(c). At the intermediate position of Fig. 13(b), the H adatom may form a hydrogen bond (blue line) with the neighboring N atom and switch the covalent bond and the hydrogen bond through the saddle-point configuration in Fig. 13(c) or through proton tunneling owing to the small proton mass and size. The distances shown by red lines in Figs. 13(b) and 13(c) are about 1.57 Å, which is the bond length of the H adatom on the surface Ga atom of the *m*-plane GaN [41]. Although precise calculations are required to evaluate $E_{\mathrm{Ga}}^{\mathrm{diff}}$ in such a situation, we guess that it is around two to three times 0.21 eV.

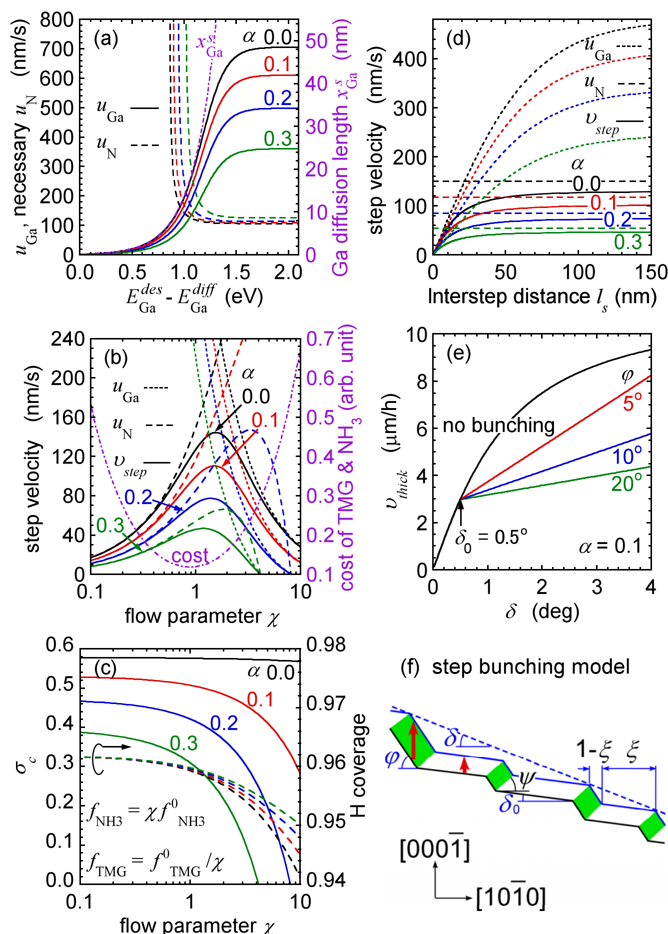

FIG. 14. Calculated results for the MOVPE growth rate of N-polar GaN. The growth conditions of the FME experiment [42] are used except for the parameter on the horizontal axes in (b)–(e). The dependencies on the decomposition factor α of NH_3 gas are shown in (a)–(d). (a) u_{Ga} (solid line) and u_{N} (dashed line) that are required to reproduce the step velocity of 99 nm/s, as functions of $E_{\mathrm{Ga}}^{\mathrm{des}}$–$E_{\mathrm{Ga}}^{\mathrm{diff}}$. x_{Ga}^{s} (chained line) is also shown. (b) υ_{step} (solid line), u_{Ga} (dotted line), u_{N} (dashed line), and cost of source materials (chained line) as functions of the flow parameter χ, where the NH_3 flow is χ times 0.067 mol/min and the TMG flow is $1/\chi$ times 21 μmol/min. (c) Degree of supersaturation σ_c (solid line) and H-adatom coverage (dashed line) as functions of χ. (d) Step velocities as functions of interstep distance l_s. (e) Thickness growth rate as a function of offcut angle δ. (f) Model of step bunching used in the calculations shown in (e): the uniform vicinal surface (dashed line) is divided into the step-bunching areas of slope φ and the scattering areas of slope δ_0 (solid line).

In the present study, the possible range of $E_{\mathrm{Ga}}^{\mathrm{diff}}$ that is consistent with the FME experiment [42] is estimated as follows. Both $\theta_{\mathrm{Ga}}^{\mathrm{T1}\infty}$ given by Eq. (B2a) and τ_{Ga} contain the same exponential factor of $\gamma_{\mathrm{Ga}}^{\mathrm{T1}} E_{\mathrm{Ga\text{-}N}}^{\mathrm{bond}}$, which is canceled in $\theta_{\mathrm{Ga}}^{\mathrm{T1}\infty}/\tau_{\mathrm{Ga}}$ because $R_{\mathrm{Ga}}^{\mathrm{T1}}$ in Eq. (B4) is negligible. Therefore, $\theta_{\mathrm{Ga}}^{\mathrm{T1}\infty}/\tau_{\mathrm{Ga}}$ in Eq. (30) is independent of the unknown parameter $\gamma_{\mathrm{Ga}}^{\mathrm{T1}}$. The remaining unknown parameter in u_{Ga} given by Eq. (30) is x_{Ga}^{s}, which is a function of $E_{\mathrm{Ga}}^{\mathrm{des}} - E_{\mathrm{Ga}}^{\mathrm{diff}}$. That is to say, although both $E_{\mathrm{Ga}}^{\mathrm{des}}$ and $E_{\mathrm{Ga}}^{\mathrm{diff}}$ are unknown, u_{Ga} depends only on their difference. Figure 14(a) shows u_{Ga} and x_{Ga}^{s} as functions of $E_{\mathrm{Ga}}^{\mathrm{des}} - E_{\mathrm{Ga}}^{\mathrm{diff}}$ under the growth condition of the

FME experiment at a high TMG flow rate. If $x^s_{\rm Ga}$ is much smaller than l_s, then the hyperbolic tangent in Eq. (30) is unity and $u_{\rm Ga}$ is proportional to $x^s_{\rm Ga}$, as shown in Fig. 14(a). On the other hand, if $x^s_{\rm Ga}$ is much larger than l_s, then $x^s_{\rm Ga}$ in Eq. (30) is canceled and $u_{\rm Ga}$ becomes independent of $E^{\rm des}_{\rm Ga} - E^{\rm diff}_{\rm Ga}$, as shown in Fig. 14(a). In this limit, $u_{\rm Ga}$ and $\upsilon_{\rm step}$ as well as σ_c are independent of the unknown parameter $\gamma^{\rm T1}_{\rm Ga}$. In Fig. 14(a), $u_{\rm N}$ required to reproduce a step velocity of 99 nm/s is also shown. For consistency with the experiment, $E^{\rm des}_{\rm Ga} - E^{\rm diff}_{\rm Ga}$ must be larger than about 0.9 eV. Therefore, $E^{\rm diff}_{\rm Ga}$ must be smaller than $E^{\rm des}_{\rm Ga} - 0.9$ eV. When $E^{\rm des}_{\rm Ga} - E^{\rm diff}_{\rm Ga}$ is 1.2 eV and α is 0.1, $\eta_{\rm NH_3}/d_k$ in Eq. (20) must be 3.6×10^{-4} nm^{-1} to reproduce the step velocity. If d_k is 10 nm, $\eta_{\rm NH_3}$ is 3.6×10^{-3}, which is identical with $\exp(-E_a/k_{\rm B}T)$ at $E_a = 0.62$ eV. E_a can be regarded as an energy barrier for the dissociative adsorption of NH_3. Although the surface structure is different, the energy barrier for the dissociative adsorption of NH_3 on the Si(001) dimer has been calculated as 0.65 eV [45]. The incident flux of NH_3 into the area Ω of a kink is 8.1×10^6 s^{-1} at the NH_3 pressure of the experiment and $\alpha = 0$. On the other hand, the incident flux of Ga gas into Ω is only 1.3×10^3 s^{-1} at the Ga pressure during the high-flow-rate period and $\alpha = 0$. If the same method as used in the case of NH_3 is applied to calculate $u_{\rm Ga}$, then $\eta_{\rm Ga}/d_k$ larger than 1.5 nm^{-1} is necessary to let $u_{\rm Ga}$ be larger than 99 nm/s. Even if $\eta_{\rm Ga}$ is assumed to be unity, d_k should be smaller than about $2a$, which is too small. This indicates that the direct Ga incorporation from gas into the kinks is not enough to reproduce the observed growth rate unless the step and kink densities increase significantly as a result of surface roughening. Ga-adatom collection from the terraces into the kinks is necessary for well-controlled step-flow growth. In this way, the observed growth rate can be reproduced by the calculations with some permissible assumptions about the unknown parameters and the formulas. It is expected that further theoretical studies and experiments under various growth conditions will provide more precise information.

F. V/III flow ratio for maximum growth rate

Optimization of the V/III flow ratio is often performed at constant $f_{\rm NH_3}$ or constant $f_{\rm TMG}$ with the other being varied. However, this method may lead to a misunderstanding owing to the effect of variations in σ_c. It is probable that σ_c affects growth mode, surface morphology, and d_k. Therefore, it is sensible to retain the same σ_c value when comparing the V-rich and III-rich conditions. From Eq. (29), σ_c is conserved when $p^2_{\rm H_2}/(p_{\rm Ga}p_{\rm NH_3}\theta^{\rm T1\infty}_{\rm H})$ is constant. In an actual growth process by MOVPE, the flow rates of the gases and the total reactor pressure are controlled. Moreover, part of the NH_3 gas decomposes to N_2 and H_2 gases if $\alpha > 0$. Therefore, it is a rather complex task to control the partial pressures. In Figs. 14(b) and 14(c), $f_{\rm NH_3}$ (the flow rate of NH_3) and $f_{\rm TMG}$ (the flow rate of TMG) are varied while $f_{\rm TMG}f_{\rm NH_3}$ and $f_{\rm H_2}$ (the flow rate of H_2) are kept constant. That is to say, $f_{\rm NH_3} = \chi f^0_{\rm NH_3}$ and $f_{\rm TMG} = f^0_{\rm TMG}/\chi$, where $f^0_{\rm NH_3} = 0.067$ mol/min and $f^0_{\rm TMG} = 21$ μmol/min, i.e., the flow rate of the FME experiment [42]. In the case of $\alpha = 0$, $p_{\rm Ga}p_{\rm NH_3}/p^2_{\rm H_2} = f_{\rm TMG}f_{\rm NH_3}/f^2_{\rm H_2}$, and consequently σ_c is almost constant, as shown in Fig. 14(c), even if the V/III flow ratio is varied by a factor of 10^4. Therefore, a constant value of d_k is assumed in the following calculations. The slight decrease in σ_c at large χ is due to the decrease in $\theta^{\rm T1\infty}_{\rm H}$. The coverage of the H adatom (bare N) slightly decreases (increases) with increasing NH_3 flow, because $p_{\rm H_2}$ decreases under the constant H_2 flow and the constant total reactor pressure.

In the following calculations, $E^{\rm des}_{\rm Ga} - E^{\rm diff}_{\rm Ga}$ is assumed as 1.2 eV, which corresponds to, for example, $E^{\rm diff}_{\rm Ga} = 0.5$ eV, $E^{\rm des}_{\rm Ga} = 1.7$ eV, and $\gamma^{\rm T1}_{\rm Ga} = 0.91$. The value of $\eta_{\rm NH_3}/d_k$ is assumed as 3.6×10^{-4} nm^{-1}. Figure 14(b) shows that $\upsilon_{\rm step}$ reaches a maximum near the condition $u_{\rm Ga} = u_{\rm N}$ [33]. The estimated Ga coverage is below the equilibrium coverage with bulk metal Ga, $\theta^{\rm eq}_{\rm bulk}$, even at the highest Ga pressure ($\chi = 0.1$). The cost of the source materials shown in Fig. 14(b) is estimated as proportional to $f_{\rm NH_3} + 2500 f_{\rm TMG}$, where the price/mol of TMG is assumed to be 2500 times of that of NH_3. The growth condition of the FME experiment ($\chi = 1$) is situated near the maximum growth rate and the minimum cost condition. The production of GaN per unit cost is proportional to the growth rate divided by the cost. Furthermore, rapid growth prevents waste of source gases and waste of running cost and increases the incorporation efficiency of In for InGaN growth. This kind of analysis gives a practical criterion to select the V/III flow ratio at constant σ_c, which probably provides constant quality, if the unknown parameters are precisely evaluated.

G. Effect of substrate offcut angle

Figure 14(d) shows the step velocity as a function of the interstep distance l_s. The same parameters as the previous section (at $\chi = 1$) are used. $u_{\rm Ga}$ increases with l_s, because the territorial area to accumulate adatoms into a kink increases. However, if $l_s/2$ exceeds $x^s_{\rm Ga} = 34$ nm, the limitation by $x^s_{\rm Ga}$ begins to be effective and saturation of $u_{\rm Ga}$ occurs. On the other hand, $u_{\rm N}$ of the present model is independent of the offcut angle and the interstep distance. $\upsilon_{\rm step}$ is limited by both $u_{\rm Ga}$ and $u_{\rm N}$ and it increases with l_s and decreases with offcut angle. Figure 14(e) shows the thickness growth rate $\upsilon_{\rm thick}$ as a function of the offcut angle δ. $\upsilon_{\rm thick}$ increases with offcut angle and decreases with l_s, contrary to $\upsilon_{\rm step}$. This is because $\upsilon_{\rm thick}$ is proportional to the product of the step density and $\upsilon_{\rm step}$ as in Eq. (25). However, such a strong dependence on the offcut angle as shown by the black line in Fig. 14(e) is not usually observed in actual growth experiments. It is known that step bunching occurs if the offcut angle is large, because the interaction between steps due to the scramble for adatoms becomes stronger as the interstep distance decreases [30]. A simple morphological model of the situation after step bunching is shown in Fig. 14(f). The uniform vicinal surface of the offcut angle δ toward $[10\bar{1}0]$ (blue dashed line) is divided into the step-bunching areas of steep φ and the areas of gentle δ_0. When the fraction of the gentle slope along $[10\bar{1}0]$ is ξ, the mean slope is $\xi \tan\delta_0 + (1-\xi)\tan\varphi = \tan\delta$. Therefore,

$$\xi = (\tan\varphi - \tan\delta)/(\tan\varphi - \tan\delta_0). \tag{34}$$

Then, the growth rate of the bunched surface is represented by

$$\upsilon^{\rm bunch}_{\rm thick}(\delta) = \xi\,\upsilon_{\rm thick}(\delta_0) + (1-\xi)\upsilon_{\rm thick}(\varphi). \tag{35}$$

The lengths of the short and long red arrows in Fig. 14(f) are proportional to $\upsilon_{\rm thick}(\delta_0)$ and $\upsilon_{\rm thick}(\varphi)$, respectively. This model does not involve either the periodicity or the length scale of the step bunching: only the fraction ξ has an effect. A steady-state growth of the step-bunching surface per unit time is shown in Fig. 14(f) by the advance of the black line to blue line. The surface morphology is retained during the growth because convex corners, where the surface of slow growth rate overcomes that of fast growth rate, and concave corners, where the surface of fast growth rate overcomes that of slow growth rate, appear alternately. The angle ψ shown in Fig. 14(f) is

$$\tan\psi = \frac{\upsilon_{\rm thick}(\delta_0)\tan\varphi - \upsilon_{\rm thick}(\varphi)\tan\delta_0}{\upsilon_{\rm thick}(\varphi) - \upsilon_{\rm thick}(\delta_0)}, \tag{36}$$

which traces an intersection between adjacent slopes. This simple morphological model of step bunching can provide a mechanism for the formation of the internal structure of the ψ -inclined sheets [green area in Fig. 14(f)] that are often accompanied by modulation of concentrations such as those of alloy, dopant, and impurities [46]. Those concentrations are modified by the slope (δ_0 and φ in this model) of the growing surface. The growth rate of the bunched surface is shown in Fig. 14(e) as a function of the offcut angle δ for the cases of $\varphi = 5^\circ$, 10°, and 20°. It is assumed that step bunching occurs only when the offcut angle is larger than $\delta_0 = 0.5^\circ$. The dependence of the growth rate on the offcut angle is suppressed with increasing φ. On the other hand, spiral growth, which produces steps, raises the growth rate at small offcut angles [28]. Therefore, the striking offcut-angle dependence of the growth rate for the ideal vicinal surface in Fig. 14(e) is mostly suppressed in actual growth experiments.

IV. CONCLUSIONS

The BCF theory for the step-flow growth mode and the thermodynamic model of compound epitaxial growth of Koukitu *et al.* have been combined through the mediation of the configuration entropy of the adatoms. The competitive adsorption coverages of the group-III and H adatoms have been evaluated using the Langmuir adsorption isotherm. The T1 sites on terraces are mostly occupied by H adatoms, and the coverages of group-III adatoms are extremely small under the typical growth conditions of MOVPE for N-polar group-III nitrides. The equilibrium coverage of group-III adatoms and the equilibrium pressure of NH_3 gas have been evaluated from the conditions of Gibbs energy balance between sources and products and speed balance between group-III and N incorporation into the step kinks. The equilibrium NH_3 and group-III gas pressures required for N-polar III-nitride growth increase with increasing H_2 pressure and temperature. AlN can grow irrespective of the H_2 pressure owing to the strength of the Al–N bond. GaN growth is possible at H_2 pressures around 1 bar under typical growth conditions and can be controlled by the H_2 pressure. InN growth is highly influenced by H_2 gas and is possible at H_2 pressures lower than about 0.1 bar under typical growth conditions around 600 °C. The major roles of hydrogen are (i) providing a significant reduction in the surface energy of the N-polar group-III nitrides as a result of H adsorption, (ii) preventing condensation of group-III adatoms, (iii) reducing supersaturation and promoting step-flow growth, and (iv) modifying group-III adatom mobility. A fair agreement between the experimental and calculated growth rates is obtained when the bond energies of the adatoms with surface N atoms are reduced by about 10% from those of the bulk group-III nitrides and NH_3. A criterion for the V/III flow ratio to obtain maximum products/cost and minimum waste of the materials under a constant degree of supersaturation has been proposed.

ACKNOWLEDGMENTS

The author would like to thank Professor Takashi Matsuoka, Tohoku University, for inspiring the study of N-polar group-III nitrides growth. This work was partly supported by Japan Society for the Promotion of Science KAKENHI Grant No. JP18K04933. The atomic structures in Figs. 4, 8, and 13 were drawn by VESTA [47].

APPENDIX A: CONFIGURATION ENTROPY AND CHEMICAL POTENTIAL OF ADATOMS

First, the coverage θ_j^{Sn} is defined as the occupancy ratio at a specific type of adsorption site Sn by a specific chemical species j, which includes dangling bonds without any adsorbate. This definition is simple at the T1 site. However, the H atom has only one bond and there are two surface N atoms with dangling bonds at a B2 site. Therefore (number of H, number of bare N) at a B2 site can be (2, 0), (1, 1), (0, 2), and (0, 0). The last case means occupancy by single M. For any n of 1, 2, 3, and 4, the coverages of M, H, and a dangling bond can be defined as

$$\theta_M^{Sn} = N_M/N_S, \tag{A1a}$$

$$\theta_{\rm H}^{Sn} = N_{\rm H}/(nN_S), \tag{A1b}$$

and

$$\theta_{\rm bare}^{Sn} = N_{\rm bare}/(nN_S) = 1 - \theta_M^{Sn} - \theta_{\rm H}^{Sn}, \tag{A1c}$$

where the number of type Sn sites, adsorbed M, adsorbed H, and dangling bond are N_S, N_M, $N_{\rm H}$, and $N_{\rm bare} = n(N_S - N_M) - N_{\rm H}$, respectively.

Next, the mixing entropy of competitive adsorption between M and H at type Sn sites is calculated. After adsorption of M, N_S–N_M bare Sn sites and $n(N_S$–$N_M)$ dangling bonds remain. Further adsorption of H atoms at the dangling bonds results in the final number of the dangling bonds $N_{\rm bare}$. Therefore, the mixing entropy of the total sites is

$$S_m = k_{\rm B}\ln\left[\frac{N_S!}{(N_S - N_M)!N_M!}\frac{(N_{\rm H} + N_{\rm bare})!}{N_{\rm H}!N_{\rm bare}!}\right]. \tag{A2}$$

If the numbers of sites and adatoms are sufficiently large, the mixing entropy per site S_m/N_S is

$$s_m = -k_{\rm B}\theta_M^{Sn}\ln\left(\theta_M^{Sn}\right) - k_{\rm B}n\theta_{\rm H}^{Sn}\ln\left[\theta_{\rm H}^{Sn}\left(\theta_{\rm H}^{Sn} + \theta_{\rm bare}^{Sn}\right)^{\frac{1-n}{n}}\right]$$
$$- k_{\rm B}n\theta_{\rm bare}^{Sn}\ln\left[\theta_{\rm bare}^{Sn}\left(\theta_{\rm H}^{Sn} + \theta_{\rm bare}^{Sn}\right)^{\frac{1-n}{n}}\right], \tag{A3}$$

using Stirling's formula and substituting the coverages for the number ratios.

Finally, the configuration entropy $\partial S_m/\partial N_j$ of adatom j must be added to the chemical potential given by Eq. (11). In the calculations of the partial derivatives of S_m, N_S must be replaced with $N_M + (N_{\rm H} + N_{\rm bare})/n$. The consequent coverage-dependent chemical potentials of M and H adatoms and dangling bonds at the Sn sites are

$$\begin{aligned}\mu_M^{Sn}(T,\theta_M^{Sn}) &= \mu_M^{\circ Sn}(T) - T\frac{\partial S_m}{\partial N_M}\\ &= \mu_M^{\circ Sn}(T) + k_{\rm B}T\ln\theta_M^{Sn}, \qquad \text{(A4a)}\\ \mu_{\rm H}^{Sn}(T,\theta_{\rm H}^{Sn}) &= \mu_{\rm H}^{\circ S1}(T) - T\frac{\partial S_m}{\partial N_{\rm H}}\\ &= \mu_{\rm H}^{\circ S1}(T) + k_{\rm B}T\ln\left[\theta_{\rm H}^{Sn}\left(\theta_{\rm H}^{Sn}+\theta_{\rm bare}^{Sn}\right)^{\frac{1-n}{n}}\right], \qquad \text{(A4b)}\end{aligned}$$

and

$$\begin{aligned}\mu_{\rm bare}^{Sn}(T,\theta_{\rm bare}^{Sn}) &= -T\frac{\partial S_m}{\partial N_{\rm bare}}\\ &= k_{\rm B}T\ln\left[\theta_{\rm bare}^{Sn}\left(\theta_{\rm H}^{Sn}+\theta_{\rm bare}^{Sn}\right)^{\frac{1-n}{n}}\right], \qquad \text{(A4c)}\end{aligned}$$

respectively. In Eq. (A4b), $S1$ corresponds to T1 when Sn is B2.

APPENDIX B: LANGMUIR ADSORPTION ISOTHERM

Here the Langmuir adsorption isotherm [26,27] will be derived with an extension to treat competitive adsorption between adatoms having more than one bond, such as group-III atoms, and those having a single bond, such as H atoms. It must be noted that the present calculations ignore effects related to the electron counting rule. When M adatoms of coverage θ_M^{Sn} and H adatoms of coverage $\theta_{\rm H}^{Sn}$ adsorb on a completely bare surface from flowing M and H_2 gases of constant partial pressures, the increase in the Gibbs free energy per site is

$$\begin{aligned}\Delta g = {}& \theta_M^{Sn}\left[\mu_M^{Sn}(T,\theta_M^{Sn}) - \mu_M^{\rm gas}(T,p_M)\right]\\ &+ n\theta_{\rm H}^{Sn}\left[\mu_{\rm H}^{Sn}(T,\theta_{\rm H}^{Sn}) - \tfrac{1}{2}\mu_{\rm H_2}^{\rm gas}(T,p_{\rm H_2})\right]\\ &+ n\theta_{\rm bare}^{Sn}\mu_{\rm bare}^{Sn}(T,\theta_{\rm bare}^{Sn}), \qquad \text{(B1)}\end{aligned}$$

where $\mu_{\rm bare}^{Sn}(T,1)$ is not shown explicitly, because it is zero. In Eq. (B1), dissociative adsorption of H_2 is assumed, because the pressure and the consequent incident flux of H in equilibrium with H_2 are very small, as shown in Fig. 3(d). By replacing $\theta_{\rm bare}^{Sn}$ with $1-\theta_M^{Sn}-\theta_{\rm H}^{Sn}$, the coverages that minimize Δg are obtained from the simultaneous equations $\partial\Delta g/\partial\theta_M^{Sn} = 0$ and $\partial\Delta g/\partial\theta_{\rm H}^{Sn} = 0$ as follows:

$$\theta_M^{Sn\infty} = R_M^{Sn}/\Xi_0^{Sn}, \qquad \text{(B2a)}$$

$$\theta_{\rm H}^{Sn\infty} = R_{\rm H}^{Sn}\left(R_{\rm H}^{Sn}+1\right)^{n-1}/\Xi_0^{Sn}, \qquad \text{(B2b)}$$

and

$$\theta_{\rm bare}^{Sn\infty} = 1-\theta_M^{Sn\infty}-\theta_{\rm H}^{Sn\infty} = \left(R_{\rm H}^{Sn}+1\right)^{n-1}/\Xi_0^{Sn}, \qquad \text{(B2c)}$$

where

$$R_M^{Sn} = \frac{p_M}{p^\circ}\exp\left[\frac{\mu_M^{\circ\rm gas}(T)-\mu_M^{\circ Sn}(T)}{k_{\rm B}T}\right], \qquad \text{(B3a)}$$

$$R_{\rm H}^{Sn} = \sqrt{\frac{p_{\rm H_2}}{p^\circ}}\exp\left[\frac{\mu_{\rm H_2}^{\circ\rm gas}(T)/2-\mu_{\rm H}^{\circ S1}(T)}{k_{\rm B}T}\right], \qquad \text{(B3b)}$$

and

$$\Xi_0^{Sn} = R_M^{Sn} + \left(R_{\rm H}^{Sn}+1\right)^n. \qquad \text{(B4)}$$

Ξ_0^{Sn} is the grand partition function for a single Sn site, where gases are supplied from a reservoir. For the T1 sites, where n is unity, Eqs. (B2a)–(B2c) are the same as the Langmuir adsorption isotherm for competitive and dissociative adsorption [27]. At the coverages given by Eqs. (B2a)–(B2c), it is confirmed using Eqs. (A4a)–(A4c) that

$$\begin{aligned}&\mu_M^{\rm gas}(T,p_M) - \mu_M^{Sn}(T,\theta_M^{Sn\infty})\\ &= n\left[\tfrac{1}{2}\mu_{\rm H_2}^{\rm gas}(T,p_{\rm H_2}) - \mu_{\rm H}^{Sn}(T,\theta_{\rm H}^{Sn\infty})\right]\\ &= n\left[\mu_{\rm bare}^{Sn}(T,1) - \mu_{\rm bare}^{Sn}(T,\theta_{\rm bare}^{Sn\infty})\right]\\ &= k_{\rm B}T\ln\Xi_0^{Sn} > 0 \qquad \text{(B5)}\end{aligned}$$

is fulfilled. Equation (B5) shows that all of the adsorbed species release the same free energy per site to reach the minimum free energy under the constraint $\theta_M^{Sn}+\theta_{\rm H}^{Sn}+\theta_{\rm bare}^{Sn} = 1$. In other words, the coverages are adjusted to fulfill Eq. (B5) according to the partial pressures and the temperature. By using Eq. (B5), Δg at the minimum is obtained as

$$\Delta g_{\rm min} = -k_{\rm B}T\ln\Xi_0^{Sn} < 0. \qquad \text{(B6)}$$

The grand partition function for all N_S adsorption sites is $(\Xi_0^{Sn})^{N_s}$ if the interaction between adatoms can be ignored. The coverages can be calculated as [48]

$$\theta_M^{Sn\infty} = \frac{k_{\rm B}T}{N_s}\frac{\partial\ln\left(\Xi_0^{Sn}\right)^{N_s}}{\partial\mu_M^{\rm gas}} \qquad \text{(B7a)}$$

and

$$\theta_{\rm H}^{Sn\infty} = \frac{k_{\rm B}T}{nN_s}\frac{\partial\ln\left(\Xi_0^{Sn}\right)^{N_s}}{\partial\left(\mu_{\rm H_2}^{\rm gas}/2\right)}. \qquad \text{(B7b)}$$

In Eq. (B7b), n appears from the definition of the H coverage. These equations provide the same results as Eqs. (B2a)–(B2c). In the same way, Eqs. (B2a)–(B2c) are easily extended to the case of quaternary competitive adsorption of Al, Ga, In, and H by replacing Ξ_0^{Sn} with $R_{\rm Al}^{Sn}+R_{\rm Ga}^{Sn}+R_{\rm In}^{Sn}+(R_{\rm H}^{Sn}+1)^n$. Similarly, the coverages of ternary (e.g., Ga, In, and H) competitive adsorption can also be formulated.

APPENDIX C: ADSORPTION OF NH_x AND H AT Gn SITES

The chemical potential $\mu_j^{\circ Gn}(T)$ for $j = $ N and H is given by Eq. (11). In the cases of NH and NH_2 adsorption, the composite-type approximation

$$\mu_{NH_x}^{\circ Gn}(T) \cong \mu_N^{\circ Gn}(T) + x\mu_H^{\circ T1}(T) \tag{C1}$$

is used. This is probably a fair approximation, because the mass of NH_x is not so different from that of N in the rough estimation of the vibrational temperatures in the Supplemental Material II [36]. Of course γ_N^{Gn} and γ_H^{T1} for Eq. (C1) must be different from those of the N adatoms at Gn and the H adatoms at T1. However, they are unknown and fixed at 0.9 in Fig. 7. In the calculations of the coverages of NH_x, Eqs. (B2a) and (B3a) are modified as

$$\theta_{NH_x}^{Gn\infty} = R_{NH_x}^{Gn}/\Xi_0^{Gn} \tag{C2}$$

and

$$R_{NH_x}^{Gn} = \frac{p_{NH_3}}{p^\circ}\left(\frac{p^\circ}{p_{H_2}}\right)^{(3-x)/2} \times \exp\left[\frac{\mu_{NH_3}^{\circ gas}(T) - (3-x)\mu_{H_2}^{\circ gas}(T)/2 - \mu_{NH_x}^{\circ Gn}(T)}{k_B T}\right] \cong R_N^{Gn}\left(R_H^{T1}\right)^x, \tag{C3}$$

where

$$\Xi_0^{Gn} = R_N^{Gn} + R_{NH}^{Gn} + R_{NH_2}^{Gn} + \left(R_H^{Gn} + 1\right)^n \tag{C4}$$

and $x = 0,\ 1,$ and 2. The last line of Eq. (C3) is obtained using Eq. (C1). The denominators for $\theta_H^{Gn\infty}$ and $\theta_{bare}^{Gn\infty}$ in Eqs. (B2b) and (B2c) must also be replaced with Ξ_0^{Gn}. In the case of the G3 sites, $R_{NH_2}^{G3}$ is omitted, because an adsorbed N atom would have five bonds. It is assumed in Eq. (C3) that the NH_x adsorbate is provided by the dissociative adsorption of NH_3 accompanied by the associative release of $(3-x)/2H_2$ molecules, because the pressure of NH_x in equilibrium [at the intersection of the thick black line and the red line in Figs. 3(f)–3(h)] with NH_3–$(3-x)/2H_2$ is very small. Furthermore, the adsorbed NH_3 probably has smaller dissociation energy barriers than those in the gas. Additionally, NH_3–$(3-x)/2H_2$ (red line) have higher chemical potential, which is suitable as source and released gases for the adsorption and growth reactions, than $1/2\ N_2$ and $x/2\ H_2$ (blue line) at the usual growth temperatures.

It must be noted that the coverages of NH and N adatoms at the G3 sites [Figs. 7(d) and 7(e)] should be the same as those of H adatoms and dangling bonds at the T1 sites [Figs. 5(c) and 5(d)], respectively, because the coverages of other kinds of adsorbates at G3 and T1 are negligible and the compared pairs represent the same situation. This requirement is fulfilled when Eq. (C1) is used (compare the lines of NH and N at G3 with the solid lines of H and bare at T1), because the relation $\theta_{NH_{x+1}}^{Gn\infty}/\theta_{NH_x}^{Gn\infty} = R_{NH_{x+1}}^{Gn}/R_{NH_x}^{Gn} \cong R_H^{T1}/1 = \theta_H^{T1\infty}/\theta_{bare}^{T1\infty}$ is obtained from Eqs. (B2b), (B2c), (C2), and (C3) when all the γ_j^{Sn}s are the same. Another thing to be noted is that the adsorption of two or more H atoms at a G2 site or a G3 site is inhibited owing to the long H–Ga bond (1.57 Å), while it is possible at a B2 site owing to the short H–N bond (1.02 Å) [41]. However, the former rarely happens and does not spoil the results, thanks to the much lower coverage of H adatoms compared with that of dangling bonds at the G2 and G3 sites, as shown in Fig. 7.

APPENDIX D: REPLACEMENT OF SOURCE Ga BY GaH

Very recent first-principles calculations have deduced that GaH is the major resultant species in the gas phase after TMG decomposition during MOVPE [49]. Here, replacement of Ga by GaH as group-III source gas is briefly discussed. The chemical potentials of the AlH and GaH gases are obtained from Refs. [34] and [50], respectively. $\mu_{MH}^{\circ gas} - \mu_{H_2}^{\circ gas}/2$ is plotted in Figs. 3(a) and 3(b) by the purple line. $\mu_{GaH}^{\circ gas} - \mu_{H_2}^{\circ gas}/2$ is higher than $\mu_{Ga}^{\circ gas}$ above 1200 K. However, the concentration of GaH gas may exceed that of Ga gas owing to the decomposition barrier [49]. The same is true for the case of the NH_3 gas and the $N_2/2 + 3H_2/2$ gases shown in Fig. 3(e). The NH_3 gas, which is necessary for GaN and InN growth, remains thanks to the large decomposition barrier of NH_3 in the gas phase. When GaH is the resultant species, $\mu_{Ga}^{gas}(T, p_{Ga})$ in Eq. (B1) must be replaced by $\mu_{GaH}^{gas}(T, p_{GaH}) - \mu_{H_2}^{gas}(T, p_{H_2})/2$. Accordingly, R_{Ga}^{Sn} in Eqs. (B2a) and (B4) must be replaced by

$$R_{GaH}^{Sn} = \frac{p_{GaH}}{\sqrt{p_{H_2}p^\circ}}\exp\left[\frac{\mu_{GaH}^{\circ gas}(T) - \mu_{H_2}^{\circ gas}(T)/2 - \mu_{Ga}^{\circ Sn}(T)}{k_B T}\right]. \tag{D1}$$

$\mu_{GaH}^{\circ gas} - \mu_{H_2}^{\circ gas}/2$ is higher than $\mu_{Ga}^{\circ gas}$ by as much as about 0.046 eV at 1015 °C. Then $\theta_{Ga}^{T1\infty}$ increases to about 2.6 times that for Ga gas when p_{GaH} in Eq. (D1) is identical with p_{Ga} and p_{H_2} is 0.348 bar. Also, σ_c, u_{Ga}, and u_N increase. Therefore, the growth rate of GaN becomes larger than those in Secs. III E–III G at the same adjustment parameters γ_H^{T1}, γ_{Ga}^{T1}, η_{NH_3}, and d_k. However, the fitting to the measured growth rate [42] can be recovered by adjusting the parameters. For example, by decreasing η_{NH_3}/d_k in Eq. (20), u_N can be adjusted to reproduce the measured growth rate. Further study is necessary to discuss the actual parameters and the actual flow ratio of GaH to Ga.

[1] H. Amano, N. Sawaki, I. Akasaki, and Y. Toyoda, Appl. Phys. Lett. **48**, 353 (1986).

[2] H. Amano, M. Kito, K. Hiramatsu, and I. Akasaki, Jpn. J.Appl. Phys. **28**, L2112 (1989).

[3] N. Yoshimoto, T. Matsuoka, T. Sasaki, and A. Katsui, Appl. Phys. Lett. **59**, 2251 (1991).

[4] S. Nakamura, Jpn. J. Appl. Phys. **30**, L1705 (1991).

[5] S. Nakamura, N. Iwasa, M. Senoh, and T. Mukai, Jpn. J. Appl. Phys. **31**, 1258 (1992).

[6] S. Nakamura, T. Mukai, and M. Senoh, Appl. Phys. Lett. **64**, 1687 (1994).

[7] S. Keller, C. S. Suh, Z. Chen, R. Chu, S. Rajan, N. A. Fichtenbaum, M. Furukawa, S. P. DenBaars, J. S. Speck, and U. K. Mishra, J. Appl. Phys. **103**, 033708 (2008).

[8] M. H. Wong, S. Keller, N. S. Dasgupta, D. J. Denninghoff, S. Kolluri, D. F. Brown, J. Lu, N. A. Fichtenbaum, E. Ahmadi, U. Singisetti, A. Chini, S. Rajan, S. P. DenBaars, J. S. Speck, and U. K. Mishra, Semicond. Sci. Technol. **28**, 074009 (2013).

[9] S. Keller, H. Li, M. Laurent, Y. Hu, N. Pfaff, J. Lu, D. F. Brown, N. A. Fichtenbaum, J. S. Speck, S. P. DenBaars, and U. K. Mishra, Semicond. Sci. Technol. **29**, 113001 (2014).

[10] M. Sumiya, M. Tanaka, K. Ohtsuka, S. Fuke, T. Ohnishi, I. Ohkubo, M. Yoshimoto, H. Koinuma, and M. Kawasaki, Appl. Phys. Lett. **75**, 674 (1999).

[11] M. Sumiya and S. Fuke, MRS Internet J. Nitride Semicond. Res. **9**, 1 (2004).

[12] T. Matsuoka, Y. Kobayashi, H. Takahata, T. Mitate, S. Mizuno, A. Sasaki, M. Yoshimoto, T. Ohnishi, and M. Sumiya, Phys. Status Solidi B **243**, 1446 (2006).

[13] J. Zúñiga-Pérez, V. Consonni, L. Lymperakis, X. Kong, A. Trampert, S. Fernández-Garrido, O. Brandt, H. Renevier, S. Keller, K. Hestroffer, M. R. Wagner, J. S. Reparaz, F. Akyol, S. Rajan, S. Rennesson, T. Palacios, and G. Feuillet, Appl. Phys. Rev. **3**, 041303 (2016).

[14] S. Keller, N. A. Fichtenbaum, M. Furukawa, J. S. Speck, S. P. DenBaars, and U. K. Mishra, Appl. Phys. Lett. **90**, 191908 (2007).

[15] Z. Y. Al Balushi and J. M. Redwing, Appl. Phys. Lett. **110**, 022101 (2017).

[16] K. Shojiki, T. Tanikawa, J. H. Choi, S. Kuboya, T. Hanada, R. Katayama, and T. Matsuoka, Appl. Phys. Express **8**, 061005 (2015).

[17] M. M. Sung, J. Ahn, V. Bykov, J. W. Rabalais, D. D. Koleske, and A. E. Wickenden, Phys. Rev. B **54**, 14652 (1996).

[18] J. E. Northrup and J. Neugebauer, Appl. Phys. Lett. **85**, 3429 (2004).

[19] A. Kusaba, Y. Kangawa, P. Kempisty, K. Shiraishi, K. Kakimoto, and A. Koukitu, Appl. Phys. Express **9**, 125601 (2016).

[20] A. Kusaba, Y. Kangawa, P. Kempisty, H. Valencia, K. Shiraishi, Y. Kumagai, K. Kakimoto, and A. Koukitu, Jpn. J. Appl. Phys. **56**, 070304 (2017).

[21] A. Koukitu, N. Takahashi, T. Taki, and H. Seki, Jpn. J. Appl. Phys. **35**, L673 (1996); A. Koukitu and H. Seki, *ibid.* **36**, L750 (1997).

[22] W. K. Burton, N. Cabrera, and F. C. Frank, Philos. Trans. R. Soc. London Sect. A **243**, 299 (1951).

[23] Y. Saito, *Statistical Physics of Crystal Growth* (World Scientific, Singapore, 1996), Part III.

[24] M. Uwaha, Prog. Cryst. Growth Charact. Mater. **62**, 58 (2016).

[25] D. P. Woodruff, Philos. Trans. R. Soc. London Sect. A **373**, 20140230 (2015).

[26] I. Langmuir, J. Am. Chem. Soc. **40**, 1361 (1918).

[27] R. I. Masel, *Principles of Adsorption and Reaction on Solid Surfaces* (Wiley, New York, 1996), Chap. 4.

[28] C.-H. Lin, T. Akasaka, and H. Yamamoto, Appl. Phys. Express **6**, 035503 (2013).

[29] A. R. A. Zauner, E. Aret, W. J. P. van Enckevort, J. L. Weyher, S. Porowski, and J. J. Schermer, J. Cryst. Growth **240**, 14 (2002).

[30] T. Aisaka, T. Tanikawa, T. Kimura, K. Shojiki, T. Hanada, R. Katayama, and T. Matsuoka, Jpn. J. Appl. Phys. **53**, 085501 (2014).

[31] K. Sekiguchi, H. Shirakawa, K. Chokawa, M. Araidai, Y. Kangawa, K. Kakimoto, and K. Shiraishi, Jpn. J. Appl. Phys. **56**, 04CJ04 (2017).

[32] If H and H_2 gases are in equilibrium, then $\mu_{\rm H}^{\rm gas}(T, p_{\rm H}) = \mu_{\rm H_2}^{\rm gas}(T, p_{\rm H_2})/2$. Under this condition, $p_{\rm H}=\sqrt{p_{\rm H_2}} \exp[(\mu_{\rm H_2}^{\circ \rm gas}/2 - \mu_{\rm H}^{\circ \rm gas})/(k_{\rm B}T)]$.

[33] M. Takata and A. Ookawa, J. Cryst. Growth **24-25**, 515 (1974).

[34] NIST Chemistry WebBook, see http://webbook.nist.gov/chemistry/.

[35] I. Barin, *Thermochemical Data of Pure Substances* (VCH, Weinheim, Germany, 1989).

[36] See Supplemental Material at http://link.aps.org/supplemental/10.1103/PhysRevMaterials.3.103404 for extrapolation of the chemical potentials and estimation of the vibrational temperatures of the adatoms.

[37] L. D. Landau and E. M. Lifshitz, *Statistical Physics* (Pergamon Press, Oxford, 1969), Chap. IV.

[38] Y. Kangawa, T. Ito, A. Taguchi, K. Shiraishi, and T. Ohachi, Surf. Sci. **493**, 178 (2001).

[39] A. I. Duff, L. Lymperakis, and J. Neugebauer, Phys. Status Solidi B **252**, 855 (2015).

[40] J. E. Northrup and J. Neugebauer, Phys. Rev. B **60**, R8473 (1999).

[41] J. E. Northrup, R. Di Felice, and J. Neugebauer, Phys. Rev. B **56**, R4325 (1997).

[42] C.-H. Lin, T. Akasaka, and H. Yamamoto, Jpn. J. Appl. Phys. **55**, 04EJ01 (2016).

[43] If $\theta_{\rm bare}^{\rm T1\infty}$ is fixed at 1/4 to be consistent with the electron counting rule, then $\theta_{\rm H}^{\rm T1\infty}$ decreases to 0.75. Then σ_c given by Eq. (29), $\theta_{\rm Ga}^{\rm T1\infty}$, and $u_{\rm Ga}$ also decrease. However, if $\gamma_{\rm H}^{\rm T1}$ is slightly reduced from 0.9 to 0.9 $-k_{\rm B}T \ln(0.96/0.75)/E_{\rm H-N}^{\rm bond} = 0.8936$, then σ_c, $\theta_{\rm Ga}^{\rm T1\infty}$, and $u_{\rm Ga}$ can recover from the decreases.

[44] L. Lymperakis and J. Neugebauer, Phys. Rev. B **79**, 241308(R) (2009).

[45] E. Fattal, M. R. Radeke, G. Reynolds, and E. A. Carter, J. Phys. Chem. B **101**, 8658 (1997).

[46] I. Bryan, Z. Bryan, S. Mita, A. Rice, L. Hussey, C. Shelton, J. Tweedie, J.-P. Maria, R. Collazo, and Z. Sitar, J. Cryst. Growth **451**, 65 (2016).

[47] K. Momma and F. Izumi, J. Appl. Cryst. **44**, 1272 (2011).

[48] C. Kittel and H. Kroemer, *Thermal Physics* (W. H. Freeman, San Francisco, 1980), Chap. 5.

[49] K. Sekiguchi, H. Shirakawa, K. Chokawa, M. Araidai, Y. Kangawa, K. Kakimoto, and K. Shiraishi, Jpn. J. Appl. Phys. **57**, 04FJ03 (2018).

[50] M. Tirtowidjojo and R. Pollard, J. Cryst. Growth **77**, 200 (1986).